Sensitivity-enhanced NMR 15N R1 and R1ρ relaxation experiments for the investigation of intrinsically disordered proteins at high magnetic fields

Tobias Stief, Katharina Vormann, Nils-Alexander Lakomek

Suggested Citation:
Stief, T., Vormann, K., & Lakomek, N.-A. (2024). Sensitivity-enhanced NMR 15N R1 and R1ρ relaxation experiments for the investigation of intrinsically disordered proteins at high magnetic fields. Methods, 223, 1–15. https://doi.org/10.1016/j.ymeth.2024.01.008

Methods 223 (2024) 1–15

Contents lists available at ScienceDirect

Methods

journal homepage: www.elsevier.com/locate/ymeth

Sensitivity-enhanced NMR ^{15}N R_1 and $R_{1\rho}$ relaxation experiments for the investigation of intrinsically disordered proteins at high magnetic fields

Tobias Stief [a,b], Katharina Vormann [a,b], Nils-Alexander Lakomek [a,b,*]

[a] Institute of Biological Information Processing (IBI-7), Forschungszentrum Jülich, Jülich, Germany
[b] Institute of Physical Biology, Faculty of Mathematics and Natural Sciences, Heinrich Heine University Düsseldorf, Düsseldorf, Germany

ARTICLE INFO

Keywords:
NMR
Relaxation measurements
Protein dynamics
Intrinsically disordered proteins
Sensitivity-enhanced HSQC
Protein backbone

ABSTRACT

NMR relaxation experiments provide residue-specific insights into the structural dynamics of proteins. Here, we present an optimized set of sensitivity-enhanced ^{15}N R_1 and $R_{1\rho}$ relaxation experiments applicable to fully protonated proteins. The NMR pulse sequences are conceptually similar to the set of TROSY-based sequences and their HSQC counterpart (Lakomek et al., J. Biomol. NMR 2012). Instead of the TROSY read-out scheme, a sensitivity-enhanced HSQC read-out scheme is used, with improved and easier optimized water suppression. The presented pulse sequences are applied on the cytoplasmic domain of the SNARE protein Synpatobrevin-2 (Syb-2), which is intrinsically disordered in its monomeric pre-fusion state. A two-fold increase in the obtained signal-to-noise ratio is observed for this intrinsically disordered protein, therefore offering a four-fold reduction of measurement time compared to the TROSY-detected version. The inter-scan recovery delay can be shortened to two seconds. Pulse sequences were tested at 600 MHz and 1200 MHz ^{1}H Larmor frequency, thus applicable over a wide magnetic field range. A comparison between protonated and deuterated protein samples reveals high agreement, indicating that reliable ^{15}N R_1 and $R_{1\rho}$ rate constants can be extracted for fully protonated and deuterated samples. The presented pulse sequences will benefit not only for IDPs but also for an entire range of low and medium-sized proteins.

1. Introduction

Intrinsically disordered proteins (IDPs), or proteins with intrinsically disordered regions (IDRs), compose about 30 % of the human proteome and fulfill essential functions in cellular regulation and signaling [1–4]. They are characterized by high disorder and increased structural dynamics, resulting in high local mobility and flexibility, allowing them to fold and adapt to various binding partners [5–7]. Recently, IDPs have received increased attention as they are involved in organizing membrane-less organelles [8–13]. Misfolding of IDPs can lead to several diseases, including neurodegenerative diseases [14–17]. Characterizing the structural dynamics of intrinsically disordered proteins is critical to a deeper understanding of their function, conformational space, and binding interactions [18,19]. The high internal dynamics of IDPs pose challenges to state-of-the-art structural biology techniques such as X-ray crystallography or cryo-EM due to diffuse electron density. NMR spectroscopy is, however, well suited to studying IDPs and their conformational dynamics [5,7,20–22].

^{15}N relaxation experiments are the "working horse" for a protein dynamics investigation by NMR spectroscopy. The original "standard" NMR ^{15}N relaxation methods, developed in the early 1990 s, cover the ps-ns time range faster than the overall tumbling rotational correlation time of the molecule [23–30]. Several sophisticated extensions were developed, e.g., *relaxation dispersion* experiments, which are sensitive to modulations of the isotropic part of the chemical shift tensor and can provide insights into the µs-ms time range [31–37]. Applications of NMR relaxation and relaxation dispersion experiments have led to numerous insights into protein structural dynamics, shaping our current understanding of the protein energy landscape [5,38–42], but also for RNA [43–45].

This manuscript focuses on the "standard" ^{15}N NMR relaxation methods addressing dynamics on the ps-ns time range, which can be considered as the flexibility of the protein. For these standard methods, several improvements have been added [25,27,46–53]. Systematic errors of used pulse sequences must be minimized to guarantee a reliable characterization of protein dynamics. This is particularly acute for IDPs

* Corresponding author at: Heinrich-Heine-Universität Düsseldorf, Institut für Physikalische Biologie (IPB), Gebäude 26.44, Ebene U1, Universitätsstraße 1, 40225 Düsseldorf, Germany. Forschungszentrum Jülich, IBI-7: Strukturbiochemie, Gebäude 05.8v, Wilhelm-Johnen-Strasse, 52425 Jülich, Germany.
E-mail addresses: n.lakomek@fz-juelich.de, Nils-Alexander.Lakomek@hhu.de (N.-A. Lakomek).

https://doi.org/10.1016/j.ymeth.2024.01.008
Received 19 July 2023; Received in revised form 21 December 2023; Accepted 16 January 2024
Available online 17 January 2024

as they are characterized by small relaxation rate constants and a high dynamic range.

Due to the long history of NMR relaxation experiments, most pulse sequences have been developed at magnetic field strengths of 14.1 T, corresponding to a ^{1}H Larmor frequency of 600 MHz and lower. Frequently, these experiments have been designed for and tested on small, well-folded globular proteins. Advances in magnet technology have led to the development of increasing magnetic field strengths of NMR spectrometers, with a 28 T magnet (1200 MHz ^{1}H Larmor frequency) recently becoming commercially available [54]. These high field strengths offer unprecedented resolution and new opportunities for investigating protein dynamics by NMR. They are particularly beneficial for studying IDPs (because of their narrow signal dispersion in the ^{1}H dimension). At the same time, high field strengths put new demands on underlying spectrometer electronics and probe design, as well as NMR pulse sequence design. Existing methods have to be tested and may have to be adapted, and novel NMR methods will be developed.

In the following, we introduce two optimized ^{15}N R_1 and $R_{1\rho}$ pulse schemes with sensitivity-enhanced HSQC detection. The presented pulse schemes have been tested at 14.1 T and 28 T magnets, corresponding to ^{1}H Larmor frequencies of 600 MHz and 1200 MHz, respectively.

Because research on IDPs represents a highly active and growing field within biomolecular solution NMR [5,7,20–22], we have tested the presented pulse sequences on an IDP, the vesicular SNARE protein Synaptobrevin-2 (Syb-2), which in its monomeric pre-fusion state behaves as an IDP [55–57]. Due to the small relaxation rate constants of IDPs, even small systematic errors of less than 1 s^{-1} will lead to substantial percentage-wise errors in rate constants. Therefore, IDPs present an ideal test case for NMR relaxation experiments and will identify even small systematic errors in the used pulse sequence. We have tested the optimized sensitivity-enhanced ^{15}N R_1 and $R_{1\rho}$ pulse sequences both at 600 MHz and 1200 MHz, using both a fully protonated as well as a deuterated sample, and compared the results to the original TROSY-based sequences, which had been tested on deuterated GB3 and 600 MHz [51]. For both fully protonated and deuterated samples, we find a high reproducibility and robustness at both field's strengths, suggesting that the presented sensitivity-enhanced sequences, as well as the original TROSY-based sequences [51], will also be applicable at any magnetic field strength between 14.1 T and 28 T. High agreement of extracted relaxation rate constants, measured either by the sensitivity-enhanced HSQC-detected or the TROSY-detected sequence, is observed. Independent of HSQC- or TROSY-detection, we also find high agreement between the protonated and the deuterated samples.

2. Materials and methods

2.1. NMR sample preparation

The gene base sequence encoding Synaptobrevin-2 (1–96), Syb-2 (1–96), the soluble part of Syb-2 (wt) without the transmembrane region, from *Rattus norvegicus* (UniProt accession number: P63045, 96 amino acids, 10.52 kDa) was codon-optimized for expression in *E. coli* and subcloned in a pET28a(+) vector. To facilitate protein isolation, a *hexa*-histidine tag was included at the N-terminus. Additionally, a Thrombin-cleavage side (amino acid sequence: LVPR'GS) was inserted for tag removal.

The pET28a(+)-His-Syb-2(1–96) plasmid was transformed into chemically competent *E. coli* BL21 (DE3) cells. Protein expression and purification followed protocols by Pobbati et al. [57,58]. Briefly, for precultures, cells were grown at 37 °C in 2xYT medium (Thermo Fisher, Waltham, MA, USA) overnight. For isotope labeling of ^{15}N Syb-2 (1–96), cells were grown in M9 minimal medium supplemented with ^{15}N-NH_4-Cl (99 %, Cambridge Isotope Laboratories, USA) as a single source for protein synthesis. The main culture was incubated at 37 °C until an OD_{600} of 0.8 was reached; at this point, protein expression was induced with 0.5 mM IPTG. Cultures were incubated at 20 °C after induction of expression for 18 h. Bacterial cells were harvested for 10 min at 6,000 x g (4 °C) using centrifugation. The cell pellet was resuspended in 20 mM HEPES (pH 7.4), 500 mM NaCl, 8 mM Imidazole, and 0.1 mM TCEP supplemented with protease inhibitors (Complete, Roche) and DNAse I for nucleic acid digestion. Cells were lysed for 20 min by sonication, followed by an additional centrifugation step for 30 min at 45,000 rpm (4 °C). The lysate was purified by Ni^{2+}-NTA affinity chromatography. His-tagged Syb-2 (1–96) was eluted with 20 mM HEPES (pH 7.4), 500 mM NaCl, 400 mM Imidazole, and 0.1 mM TCEP. Thrombin cleavage was combined with dialysis overnight at 4 °C in 20 mM HEPES (pH 7.4), 150 mM NaCl, 0.1 mM TCEP, and 1 mM EDTA. Thrombin was separated from digested protein by ion exchange chromatography using 20 mM HEPES (pH 7.4), 0.1 mM TCEP, 1 mM EDTA, and a Resource Q column (Cytiva, Marlborough, MA, USA) for isolation. For elution, the same buffer composition was used with 1000 mM NaCl added. To increase the purity of the sample, a size exclusion chromatography was performed afterward using a HighLoad 16/600 Superdex 75 pg column (Cytiva, USA) equilibrated in 50 mM MES (pH 6.0), 150 mM NaCl, 0.1 mM TCEP and 1 mM EDTA.

For the expression of deuterated ^{2}H^{15}N^{13}C Syb-2 (1–96) and ^{2}H^{15}N Syb-2 (1–96), commonly used filtered and deionized water (Milli-Q, Merck, USA) was replaced by D_2O. To reduce stressing conditions for cell growth, the transition from 2xYT medium into minimal medium with D_2O was performed slowly. First, cells were precultured in 2xYT medium and ddH_2O at 37 °C overnight. Then, cells were precultured in M9 minimal medium supplemented with ^{15}N-NH_4-Cl in ddH_2O at 37 °C for 8 h. In the third overnight preculture, ddH_2O was replaced by D_2O. The main culture of deuterated ^{2}H^{15}N^{13}C Syb-2 (1–96) was supplemented with ^{15}N-NH_4-Cl and ^{13}C-D-glucose (99 % Cambridge Isotope Laboratories, USA) in D_2O. The main culture of deuterated ^{2}H^{15}N Syb-2 (1–96) was supplemented with ^{15}N-NH_4-Cl in D_2O. Induction of expression with IPTG and protein isolation was performed as described for ^{15}N Syb-2 (1–96); see above.

2.2. NMR spectroscopy

2.2.1. Potential sources of artifacts in standard NMR relaxation experiments

Well-known systematic errors are generated by cross-correlated relaxation (CCR) of the ^{1}H-^{15}N dipolar coupling (DD) and the ^{15}N chemical shift anisotropy (CSA) [27,46,48], which increases at higher magnetic fields [52]. Refocusing of the respective CCR during the NMR relaxation period is usually achieved by 180° ^{1}H pulses [27]. For several ^{15}N R_1 experiments, frequently, a train of hard 180° ^{1}H pulses, spaced by a 5 ms delay, was used to suppress CCR. As discussed in the earlier work on ^{15}N NMR relaxation experiments with TROSY-detection [51], this pulse train leads, however, to partial saturation of the water magnetization. The degree of water saturation will vary depending on the length of the relaxation period. In combination with the long T_1 times of the water in the order of 3–4 s, this can substantially attenuate the available amide proton magnetization via direct exchange with the water magnetization or through ^{1}H–^{1}H NOEs to nearby exchangeable protons [51], as also pointed out by Chen and Tjandra independently [50]. The impact of progressive water saturation during the ^{15}N T_1 relaxation period increased the measured ^{15}N R_1 rate constant and was discussed in detail in [51]. This apparent (artificial) increase could be correlated to the solvent exposure of the respective amide group, with the most solvent-exposed amide groups displaying the strongest increase [51]. That systematic error can be circumvented by choosing very long interscan recovery delays (up to 10 s), leading to very long experimental times that are frequently not affordable. Another possibility is to saturate the water resonance entirely before the relaxation period starts, resulting in intensity losses for amide groups subject to solvent exchange. As discussed in the context of the TROSY-based sequences [51], shaped I-BURP-2 180° ^{1}H pulses, being selective on the amide protons and spaced by a 40 ms delay, provide an alternative [51]. The 40 ms

inter-pulse delay was sufficient to refocus CCR but, simultaneously (in combination with amide-selective shaped pulses), disturbs the water magnetization only minimally. We use the same strategy for the sensitivity-enhanced HSQC-detection scheme (Fig. 1). As pointed out, the key is keeping or returning the water magnetization to the z-axis. This is also achieved by the additional ^{1}H 90(-x) pulse at the end of the refocused INEPT transfer, which fulfills two purposes: Returning the water to the z-axis and removing any residual antiphase coherence.

Radiation damping of the water magnetization [59] is an additional but related concern, particularly acute for cryoprobes and high-field magnetics [60–62]. Very weak gradients can dephase the water magnetization and prevent radiation damping [63]. An alternative is to return the water magnetization to the z-axis using water-flip back pulses [49,62,64]. The TROSY-based- and HSQC-based experiments (Fig. 1, see below) have been designed to return the water magnetization to the z-axis in the refocused ^{1}H-^{15}N INEPT transfer before the relaxation period. Therefore, the water magnetization is aligned along the z-axis at the start of the relaxation period. The R_1 relaxation delay element is designed to disturb the water magnetization minimally (see above).

For the $R_{1\rho}$ relaxation period, we introduce amide-selective IBURP-2 pulses, which will be discussed further below. Therefore, systematic errors due to varying degrees of water saturation will be alleviated in the examined sequences. Any disturbance of the water magnetization after the relaxation period will reduce the achievable signal-to-noise ratio of the NMR experiment but will not introduce additional systematic errors.

The TROSY detection element is advantageous regarding water suppression, as decoupling on the ^{1}H channel during t_1 evolution is avoided; for the sensitivity-enhanced HSQC detected relaxation experiments, a 180° (^{1}H) is used to refocus J-coupling evolution. A second 180° (^{1}H) pulse at the beginning of the t_1 evolution is used within the gradient-based Echo-/ Anti-Echo encoding element. The water magnetization will be returned to the z-axis after the second 180° (^{1}H) pulse. Radiation damping can occur in principle for longer t_1 times and the associated spacing of the two 180° (^{1}H) pulses. Although at the two spectrometers tested, we did not observe strong radiation damping, an optional weak rectangular gradient (<2%) can be included in the pulse sequence (Fig. 1, gradient G10, grey) to prevent radiation damping [63], similarly as used in [51]. We further minimized the impact of the water signal caused by using hard 90° and 180° ^{1}H pulses by carefully choosing gradients (Fig. 1, see below). Using amide-selective detection schemes, applied in SOFAST-HMQC or Band-selective Excitation Short-Transient (BEST) detection schemes, presents an alternative [65,66]. Very recently, during the revision of this manuscript, broad-band shaped pulses designed by optimum control theory were introduced to cover the large spectral width at very high magnetic fields [67]. Using those pulses, a significant SNR increase in a ^{1}H, ^{15}N TROSY-HSQC experiment could be obtained while requiring only moderate RF power levels.

2.2.2. General setup of NMR relaxation experiments

We have recorded NMR relaxation experiments using a 171.1 μM ^{15}N Syb-2 (1–96) sample and, for comparison, a 171.7 μM ^{2}H^{15}N Syb-2 (1–96) sample in 50 mM MES (pH 6.0) buffer containing 150 mM NaCl, 0.1 mM TCEP and 1 mM EDTA. (The ^{15}N R_1 experiment, investigating the influence of the recovery delay, had been recorded on a 210 μM ^{2}H^{15}N^{13}C Syb-2 (1–96) sample.)

All NMR experiments were performed at 278.15 K using a 250 μl volume filled in a 3 mm NMR sample tube[1]. Experiments at 600 MHz ^{1}H Larmor frequency were conducted on a Bruker 600 MHz AVANCE III HD spectrometer equipped with a Bruker 5 mm QCI ^{1}H, ^{15}N, ^{13}C, ^{31}P quadruple resonance cryoprobe. Experiments at 1200 MHz ^{1}H Larmor frequency were recorded on a Bruker 1200 MHz AVANCE NEO spectrometer (Bruker, Billerica, MA, USA) equipped with a 3 mm TCI ^{1}H, ^{15}N, ^{13}C triple resonance cryoprobe.

The optimized ^{15}N R_1 and $R_{1\rho}$ pulse sequences with sensitivity-enhanced HSQC detection presented here (Fig. 1) employ a sensitivity-enhanced HSQC detection scheme [27,68] and can be applied to fully protonated proteins. The basic building blocks of those two sequences are conceptually similar to the previous TROSY-based sequences and their HSQC counterparts, initially designed in the Bax laboratory [51]. At that time, those pulse sequences had been tested on deuterated GB3 at 600 MHz. While the TROSY-detection [69,70] offers the best water suppression by using fewer ^{1}H pulses and avoiding ^{1}H decoupling, the sensitivity-enhanced HSQC scheme provides a higher signal-to-noise ratio (SNR) in principle (up to two-fold theoretically). In the sensitivity-enhanced read-out scheme, more ^{1}H pulses are used by design. While care was taken to return the water magnetization to the z-axis by the end of the pulse sequence, radiation damping of the water magnetization during the pulse sequence and its associated water trajectory is a potential pitfall. Previously, radiating damping was (partially) avoided by the use of soft rectangular gradients (of fixed duration) placed in the delay periods, requiring, however (in our hands), a very careful and frequently tedious gradient optimization. In turn, the potential gain in SNR of the HSQC-based sequence was often limited by a still strong water signal, limiting the affordable receiver gain setting [51].

The ^{15}N R_1 and $R_{1\rho}$ pulse sequences with sensitivity-enhanced HSQC detection presented here offer an improved water suppression (see Results section, Fig. 3), and an easier to optimize water suppression (in our hands), by replacing those previous weak rectangular gradients by soft shaped gradients that can be adjusted in their gradient strengths and duration. Further, the ^{15}N $R_{1\rho}$ experiment uses two shaped ^{1}H pulses rather than two hard 180 (^{1}H) rectangular pulses spaced by a weak rectangular gradient in the delay period. To obtain the best water suppression in the sensitivity-enhanced HSQC experiments, we recommend optimization of the ^{1}H carrier frequency using a pre-saturation experiment (Bruker: zgpr sequence) and adjusting the ^{1}H carrier frequency (Bruker: o1) such that the water signal is minimized. Because of the easier-optimized water suppression combined with the high SNRs that can be achieved (see below), we anticipate these sequences to be of practical importance and valuable for various fully protonated small to medium-sized proteins.

In the following, we briefly discuss the magnetization transfer pathway of the ^{15}N R_1 and $R_{1\rho}$ pulse sequences shown in Fig. 1. After the recovery delay, a hard 90° (^{15}N) pulse destroys any residual non-Boltzmann magnetization that could be present on ^{15}N. A refocused INEPT element (two consecutive INEPT transfers [70]) transfers the initial ^{1}H Boltzmann magnetization to in-phase magnetization on the ^{15}N nucleus. During the following relaxation period, magnetization on the ^{15}N nucleus decays - depending on the length of the relaxation delay, and results in decreased intensities as a function of the relaxation delay. The observed decay of intensities will be fitted by a mono-exponential decay function later to obtain the relaxation rate constants. Residue-specific intensities and rate constants will be acquired by the following t_1 evolution period of the transverse ^{15}N magnetization. For quadrature detection (phase sensitivity in the ^{15}N dimension), ^{15}N coherences are encoded by an Echo/ Anti-Echo encoding scheme with alternating gradients [27,68]. The ^{15}N evolution period is followed by a refocused INEPT element, which transfers the magnetization to the amide protons. During a final Hahn-Echo element, the decoding gradient of the Echo/ Anti-Echo scheme follows. The complete pulse scheme is illustrated in Fig. 1. Gradients during the INEPT elements are implemented both for coherence selection and to prevent radiation damping of the water magnetization (here, only weak gradient strengths

[1] For 3 mm NMR tubes, a minimal sample volume of 150 μl is recommended. We, however, suggest the use of a slightly larger volume of about 200 μl, as for smaller volumes, we noticed difficulties of the automated shimming routine (Topshim routine on Bruker NMR spectrometers), leading to substantially increased higher-order shims (Z6 in particular) and resulting in high shim-coil temperatures. We did not notice any adverse effects on the shim symmetry when using larger sample volumes of 200 μl or 250 μl.

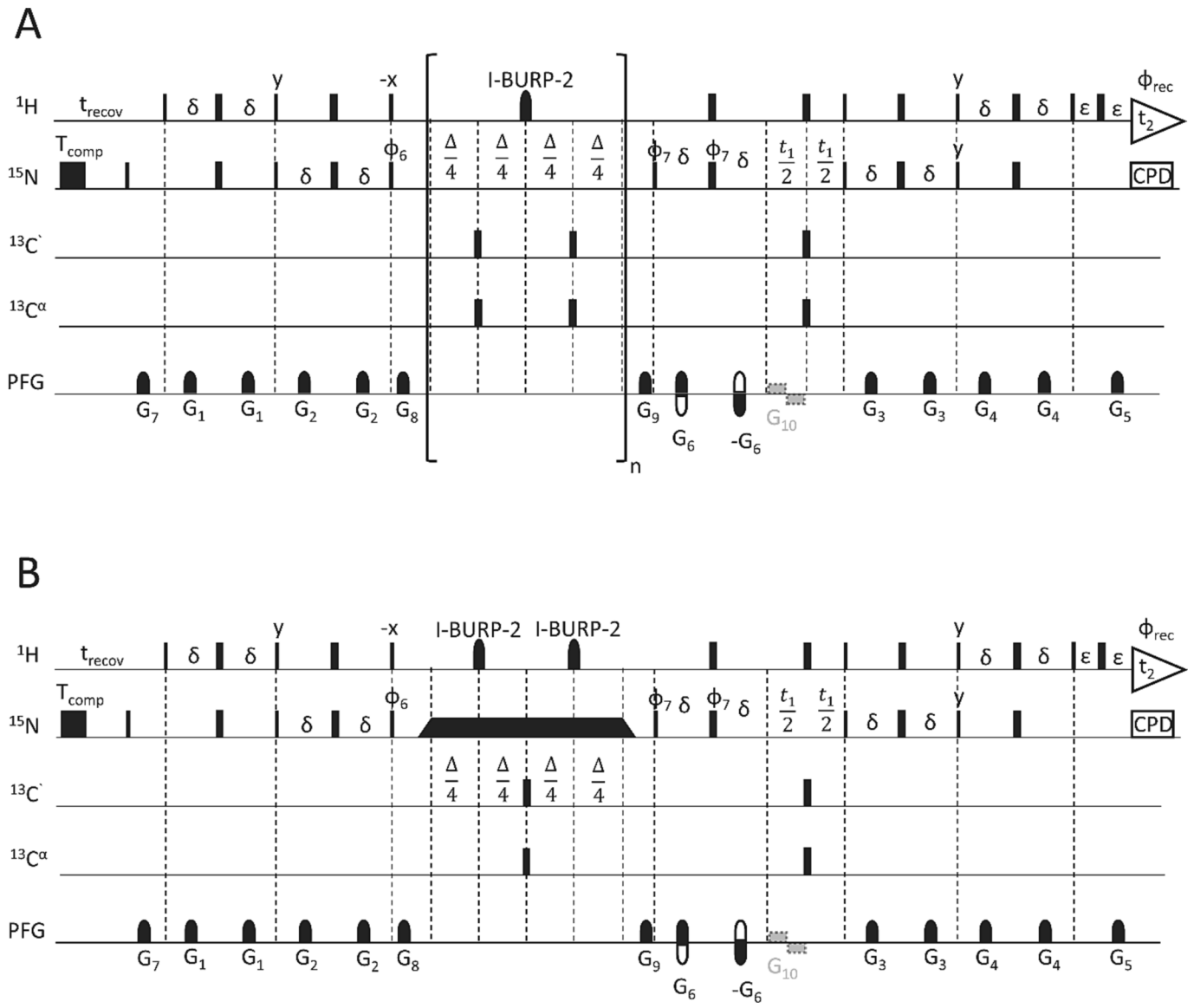

Fig. 1. Pulse sequence schemes of NMR relaxation experiments using a sensitivity-enhanced HSQC read-out scheme. The following phase cycling is applied: φ_6 = y, y, -y, -y; φ_7 = y, -y, φ_{rec} = y, -y, -y, y. The quadrature detection is implemented with the polarity inversion of the encoding gradient G_5 and the phase cycling of φ_7 (Echo/ Anti-Echo detection [27]). A: Pulse sequence scheme of the used ^{15}N R_1 relaxation experiment. Narrow rectangles correspond to 90° hard pulses with phase x, if not marked otherwise. 180° hard pulses are displayed as broad rectangles. B: Pulse sequence scheme of the used ^{15}N $R_{1\rho}$ experiment. Apart from the bracketed relaxation period, the $R_{1\rho}$ experiment is similar to the R_1 experiment.

are used) [63,71].

2.2.3. *^{15}N R_1 experiment*

The central part of pulse schemes is the relaxation period, which will be discussed in more detail in the following: In the ^{15}N R_1 experiment, the relaxation period is elongated by increasing a loop counter and the associated number of repetitions (n) of the bracketed part of the pulse scheme (Fig. 1A). The entire relaxation period is omitted in the first experiment, resulting in the $\tau_1 = 0$ reference point. Cross-correlated relaxation of the ^{15}N chemical shift anisotropy (CSA) and the ^{1}H-^{15}N dipolar coupling interactions during the relaxation period is refocused by a central I-BURP-2 180° pulse [72], selective to the amide proton resonances at $\Delta/2$, the center of the respective loop element. The relaxation loop is repeated an even number of times (n = 0, 2, …) to balance the evolution of longitudinal cross-correlated relaxation during the relaxation period Δ. These I-BURP-2 pulses invert the amide proton magnetization during the relaxation period. Here, it is essential to use selective pulses to avoid exciting the water resonance, as partial saturation of the water magnetization for more extended relaxation periods would impact the return to ^{1}H Boltzmann equilibrium adversely [49], resulting in erroneous and too high ^{15}N R_1 rate constants for solvent-exposed residues (see section 2.2.1.) [50,51]. Any amide proton will spend half of the relaxation period in the α-state and half the time in the β-state (assuming an ideal case, without any random ^{1}H–^{1}H spin-flips during the relaxation period). As a result, the longitudinal cross-correlated relaxation between the ^{1}H-^{15}N dipolar coupling and the ^{15}N chemical shift anisotropy will be averaged out.

In the following, we briefly discuss the experimental parameters of the ^{15}N R_1 experiment: The duration of the delay in the INEPT transfer is δ = 2.65 ms; the delay ∈ corresponds to the decoding gradient G4 (201 μs). This delay makes inserting the decoding gradient without adding a linear phase error to the proton dimension possible. The variable delay corresponds to the delay between two shaped 180° I-BURP-2 pulses, selective on the amide proton region. For the duration of the individual I-BURP-2 pulses, we choose a length of 1000 μs at 1200 MHz to cover the amide ^{1}H chemical shift region of the IDP Syb-2 (1–96). We used a delay

of 40 ms; the choice of the delay depends on the relaxation properties of the protein, which must be faster than the cross-correlated relaxation rate of the protein. The relaxation period is elongated by increasing the loop counter n and the associated repetition of the bracketed element of the pulse scheme. In the first experiment, the entire relaxation period will be jumped over. The relaxation loop is repeated an even number of times (n = 0, 2, …) to match the chosen relaxation delay. For the elimination of any cross-correlated relaxation between the ^{13}C and ^{15}N nuclei (applicable to ^{13}C labeled samples) on the ^{13}C channel, four 180° pulses, two selective rectangular 180° ^{13}C pulses are applied on $^{13}C'$ as well as on $^{13}C^{\alpha}$, at Δ*1/4 and Δ*3/4 of the relaxation period. The duration of the selective rectangular $^{13}C'$ pulse is chosen such that the $^{13}C^{\alpha}$ resonances are not excited and vice versa (see below) [64]. The length of these selective rectangular 180° pulses is defined by $\frac{\sqrt{3}}{2\Omega}$ [64]. Ω corresponds to the chemical shift difference between $^{13}C^{\alpha}$ and $^{13}C'$; therefore, the pulse length of the 180° pulses was set to 23.7 μs at 1200 MHz. Gradients are sine-bell shaped, identical to the sine.20 gradient shape of the Bruker gradient library, apart from G7, which is a sine.50 shaped. The gradient strengths are G_1 (200 μs, 1 % (at our spectrometer setting), corresponding to 0.58 G/cm), and G_2 (200 μs, 2 %, 1.16 G/cm), G_3 (800 μs, 31 %, 17.98 G/cm), G_4 (200 μs, 11 %, 6.38 G/cm), G_5 (201 μs, 50 %, 29.00 G/cm), G_6 (1000 μs, 50 %, 29.00 G/cm), G_7 (200 μs, 50 %, 29.00 G/cm), G_8 (200 μs, 5 %, 2.90 G/cm), and G_9 (200 μs, 14 %, 8.12 G/cm). Further, we include an optional Gradient G10 (t1/4, 0.5 %, 0.29 G/cm) during the first half of the t1 evolution period that can be switched on in case radiation damping is observed. In the ^{15}N dimension, a garp decoupling with an RF amplitude of 1.25 kHz, corresponding to a 90° pulse length of 200 μs, is applied.

For the measurements conducted at 600 MHz we used the identical gradient setup. Therefore, this gradient setup should be widely applicable to various spectrometer frequencies between 600 MHz and 1200 MHz. At least the suggested gradient setup provides a good starting point for any further (and spectrometer dependent) optimization of the water suppression.

2.2.4. ^{15}N $R_{1\rho}$ experiment

For the ^{15}N $R_{1\rho}$ experiment (Fig. 1B), providing rate constants of the transverse relaxation, R_2 (see below), an adiabatic half-passage pulse turns the ^{15}N magnetization from the z-axis to the transverse plane, or the effective field direction for off-resonance nuclei, respectively [73,74]. The adiabatic half tanh/tan pulse [74] has the same strength as the applied spin-lock RF amplitude (2 kHz). During the relaxation period, the magnetization is spin-locked in the rotating frame, and the intensity decay of the respective resonances is measured as a function of the lengths of the relaxation delay period Δ.

In principle, the RF amplitude should be as high as affordable to reduce exchange contributions and off-resonance effects at the edges of the spectrum. The higher the spectrometer frequency, the more significant potential off-resonance effects will be. At 1200 MHz, for example, a 2 kHz spin-lock RF amplitude will be equivalent to 1 kHz at 600 MHz in terms of off-resonance effects. Particular care must be taken to properly align the magnetization along the effective field axis using an adiabatic pulse with the same RF amplitude as the following spin-lock. Confirming that the adiabatic pulse fulfills its adiabaticity condition for the given RF amplitude is important. Otherwise, magnetization components orthogonal to the effective field axis will be generated that will get dephased during the initial spin-lock period, leading to a sudden intensity drop in the decay curve and, consequently, a bi- or multi-exponential decay.

During the relaxation period, two 180° I-BURP-2 pulses, selective to the amide proton resonances, are applied at Δ*1/4 and Δ*3/4 of the relaxation period to average out contributions by transverse ^{15}N chemical shift anisotropy (CSA)/^{1}H-^{15}N dipolar coupling cross-correlated relaxation. In the case of ^{13}C labeled samples, a selective soft rectangular 180° pulse is applied, one at the $^{13}C'$ and the other at the $^{13}C^{\alpha}$ carrier, to prevent any errors potentially introduced by cross-correlated relaxation between ^{15}N and ^{13}C. In both $R_{1\rho}$ and R_1 experiments, a temperature-compensation element [51] is applied off-resonance on the ^{15}N channel. On modern NMR probes, that temperature compensation element will not necessarily be required and could be switched off to reduce the power deposition in the probe, at least in our experience.

In the following, we briefly describe the setup of the ^{15}N $R_{1\rho}$ experiment: Apart from the bracketed relaxation period, the $R_{1\rho}$ experiment is similar to the R_1 experiment. The gradient setup is identical. The additional gradient G9 is a sine-bell-shaped (sine.20 Bruker gradient library), with a duration of 200 μs and a strength of 10 %, corresponding to 5.8 G/cm. (This gradient will dephase residual orthogonal magnetization. A stronger gradient is advisable but has to be adjusted as a trade-off between dephasing efficiency and good overall water suppression.) The variable delay is equal to the length of the relaxation period. A spinlock with an RF amplitude of 2 kHz is applied during the relaxation period. Before the spinlock, an adiabatic half passage pulse (AHP) with a duration of 3000 μs aligns the magnetization on the effective field axis [63], and a second AHP returns the magnetization to the z-axis after the spinlock period. Those AHPs are displayed as triangle pulses before and after the spinlock. They correspond to the first and second half of a tangent-hyperbolic tangent (tanh/tan) adiabatic inversion pulse, as defined in the Bruker pulse library (100 kHz total sweep width, ζ = 10, tan(κ) = 20, ωmax = 2 kHz). As for the R_1 experiment, 180° pulses on the $^{13}C'$ and the $^{13}C^{\alpha}$ are used to eliminate the cross-correlated effects resulting from the ^{13}C-^{15}N dipolar interactions in ^{13}C labeled samples. The two I-BURP-2 pulses stop the transverse cross-correlated relaxation contributions from the ^{15}N chemical shift anisotropy and the ^{1}H-^{15}N dipolar coupling interactions.

The optimized NMR pulse sequences can be downloaded at www.ipb.hhu.de/en/teams/team-lakomek/pulsesequences.

2.2.5. Application to intrinsically disordered proteins

To test the applicability of the pulse sequences on fully-protonated intrinsically disordered proteins and at high magnetic field strengths, we recorded ^{15}N R_1 and $R_{1\rho}$ relaxation experiments on monomeric Syb-2 (1–96), see above, which is intrinsically disordered in its monomeric state [55,57,75]. NMR spectra were acquired at 1200 MHz and 5 °C, with 16.03 ppm spectral width in the ^{1}H direct dimension and 30.02 ppm spectral width in the ^{15}N indirect dimension. Altogether, eight different relaxation delays were recorded for the ^{15}N R_1 and ^{15}N $R_{1\rho}$ experiments. Each spectrum (=plane of the pseudo-3D) was acquired with 1024 complex data points in the ^{1}H dimension, corresponding to an acquisition time of 53.25 ms in the ^{1}H dimension. In the ^{15}N dimension, experiments were performed with an acquisition time of 70.14 ms and 256 complex data points per spectrum. Frequency carriers were placed for protons at 4.690 ppm, nitrogen at 117 ppm, and carbon at 176 ppm. For the R_1 experiment, the following relaxation delays were randomly shuffled: 0 ms, 960 ms, 240 ms, 800 ms, 160 ms, 640 ms, 320 ms, and 480 ms. In the $R_{1\rho}$ experiment, the following delays were used: 5 ms, 65 ms, 25 ms, 45 ms, 15 ms, 55 ms, 35 ms, and 10 ms. The first delay serves as the reference point. For the spinlock on the ^{15}N channel, a radio frequency (RF) amplitude of 2 kHz was applied. A four-step phase cycle was employed, limiting the applicable number of scans to multiples of four. As an interscan delay, 2.0 s were used unless specified otherwise. The experiments at 1200 MHz had a duration of 12 h 12 min total for the R_1 experiment and a duration of 10 h 19 min for the $R_{1\rho}$ experiment. A detailed overview of the chosen experimental parameters is shown in Table S1. Experimental NMR parameters for the relaxation experiments recorded at 600 MHz are shown in Table S2.

For comparison, TROSY experiments were acquired as described in [51].

2.2.6. Evaluation of NMR relaxation data

To evaluate the experimental data, the dedicated NMR pipe [76] scripts originally published in the context of the TROSY-based sequences

[51] were modified slightly. Scripts can be downloaded under the following link:

www.ipb.hhu.de/en/teams/team-lakomek/pulsesequences.

The R_2 rate constants were calculated by the following formula [77,78]:

$$R_2 = \frac{R_{1\rho}}{sin^2\theta} - \frac{R_1}{tan^2\theta} \quad (1)$$

The angle $\theta = arctan\left(\frac{\omega_1}{\Omega}\right)$ represents the angle between the axis of the effective magnetic field B_{eff} and the external magnetic field B_0, ω_1 is the RF amplitude of the spin-lock and Ω the chemical shift offset (the difference between the ^{15}N chemical shift of the respective residue and the ^{15}N carrier frequency) [77,78].

The experimental error was estimated using the NMR pipe-integrated Monte-Carlo-based error analysis [76]. The signal-to-noise ratio obtained for the various experiments (cf. Table 1) was calculated by taking the mean of the intensities of the three most intense resonances in the reference spectrum (first entry in the relaxation delay list). Those signals had to be non-overlapping signals. Their average intensity was divided by the noise estimated using nmrDraw / nmrPipe scripts [75]. Further, a "weak" SNR takes the average intensity of the three least intense signals and is divided by the noise calculated with nmrDraw. All SNR values were calculated for the reference spectrum acquired with the first entry of the vplist in the $R_{1\rho}$ experiment or with the first entry of the vclist in the R_1 experiment.

3. Results and discussion

We have tested the optimized NMR relaxation experiments for their applicability to intrinsically disordered proteins. As a model system, we used the soluble cytoplasmic part of the vesicular SNARE protein Synaptobrevin-2 (1–96), frequently referred to as VAMP-2 (vesicle-associated membrane protein 2). Synaptobrevin-2 (1–96), dubbed Syb-2 (1–96), is intrinsically disordered in its monomeric pre-fusion state. As a first assessment of the IDP character of Syb-2 (1–96), we recorded two-dimensional ^1H-^{15}N HSQC spectra on ^{15}N Syb-2 (1–96), both at 600 MHz and 1200 MHz.

Table 1
Signal-to-noise comparison for the ^{15}N R_1 and R_2 ($R_{1\rho}$) NMR relaxation experiments recorded on ^1H ^{15}N Syb-2, using the sensitivity-enhanced HSQC-detection or for comparison using the TROSY-detection scheme. (A) The SNR is calculated by taking the average of the three most intense resonances. For comparison, the "weak" SNR is also calculated by taking the average of the three least intense ("weakest") resonances (B) to get a better impression of the dynamic range. A.

A

Experiment	NS	read out	Field/ MHz	SNR (strong)	ExtrapolatedSNR (at 8 NS)[1]
$R_{1\rho}$	4	HSQC	1200	688	972
$R_{1\rho}$	8	TROSY	1200	388	388
R_1	4	HSQC	1200	717	1014
R_1	8	TROSY	1200	404	404
$R_{1\rho}$	4	HSQC	600	332	469
$R_{1\rho}$	8	TROSY	600	237	237
R_1	4	HSQC	600	337	477
R_1	8	TROSY	600	228	228

B

Experiment	NS	read out	Field/ MHz	SNR (weak)	ExtrapolatedSNR (at 8 NS)[1]
$R_{1\rho}$	4	HSQC	1200	47	66
$R_{1\rho}$	8	TROSY	1200	35	35
R_1	4	HSQC	1200	55	78
R_1	8	TROSY	1200	38	38
$R_{1\rho}$	4	HSQC	600	65	91
$R_{1\rho}$	8	TROSY	600	57	57
R_1	4	HSQC	600	71	100
R_1	8	TROSY	600	57	57

[1] Extrapolated SNR: As the HSQC-detected schemes were recorded with four scans only, their measured SNR was multiplied by a factor $\sqrt{2}$, to be comparable to the TROSY-detection schemes, which were recorded with eight scans.

3.1. Comparison of ^1H-^{15}N HSQC spectra of ^{15}N Syb-2 (1–96) recorded at 600 MHz and 1200 MHz

Fig. 2 shows spectra of fully-protonated Syb-2 (1–96) measured at 600 MHz (Fig. 2A) and 1200 MHz (Fig. 2B). Both spectra have been recorded with an acquisition time of 106.5 ms in the direct ^1H dimension, corresponding to 1024 complex points in the direct ^1H dimension at 600 MHz and 2048 complex points at 1200 MHz. In the indirect ^{15}N dimension, 256 complex points were recorded. The timewise increment is defined by 1/SWH (or 1/(2*SWH), respectively, depending on the employed quadrature detection and implementation of the pulse sequence), with the spectral width in Hz dubbed SWH. Therefore, at 1200 MHz, the length of the timewise increment, 1/SWH, will be only half as long as the corresponding one at 600 MHz. Thus, the double number of increments must be recorded at 1200 MHz relative to 600 MHz to achieve the same total acquisition time and resulting spectral resolution in Hz (which correlates inversely to the total acquisition time). While a longer acquisition time in the direct ^1H dimension will minimally increase the overall experimental time, the twice-as-long acquisition time in the indirect dimension due to the doubling of the recorded complex points will double the experimental time. However, when doing so, the resolution can be further increased (Fig. 2C). As evident from Fig. 2, higher magnetic field strengths will be beneficial for recording highly resolved NMR spectra of IDPs, even when fully protonated.

3.2. ^{15}N R_1, $R_{1\rho}$ with sensitivity-enhanced HSQC-detection and improved water suppression

3.2.1. Modifications in the ^{15}N R_1 and $R_{1\rho}$ pulse sequences

We briefly reiterate the main modifications for the ^{15}N R_1 and ^{15}N $R_{1\rho}$ relaxation experiments using a sensitivity-enhanced HSQC read-out scheme: starting from the original TROSY-based NMR relaxation experiments and their HSQC counterpart [51], we have implemented ^{15}N R_1 and $R_{1\rho}$ pulse sequences using a sensitivity-enhanced (Rance-Kay) HSQC read-out scheme with improved water suppression

(Fig. 1). We emphasize that for both read-out schemes, the TROSY and the HSQC-detected ones, the "standard" ^{15}N R_1 and $R_{1\rho}$ (auto-relaxation) rate constants are measured. Relative to the original implementation (compare SI Fig. S1 in [51]), instead of weak rectangular gradients of fixed duration, we have used shorter shaped gradients that can be adjusted both in duration and time, allowing an easier to optimize water suppression. For the $R_{1\rho}$ experiment, we replaced the two hard 180° pulses (plus the soft gradient in between, preventing radiation damping) with two shaped I-BURP-2 pulses, which are selective on the amide protons. Fig. 1 shows the improved set of NMR R_1 and $R_{1\rho}$ relaxation pulse sequences with sensitivity-enhanced (Rance-Kay) HSQC detection and improved water suppression, applicable at high-field magnets. We refer to the Materials and Methods section for details on the experimental setup.

3.2.2. Improved water suppression

Fig. 3 displays the improved water suppression obtained using the presented ^{15}N R_1 and $R_{1\rho}$ NMR relaxation experiments with sensitivity-enhanced HSQC detection, tested both at 1200 MHz and 600 MHz. For comparison, the water-suppression using the previous implementation (SI Fig. S1 in [51]) is shown [51]. The water-suppression obtained for the deuterated Syb-2 sample (see below) is shown in Fig. S2. Apart from the ^{15}N R_1 experiment at 600 MHz, the level of water suppression of the new implementation is improved compared to the previous implementation. At 1200 MHz, using a 3 mm Bruker TCI cryoprobe, the level

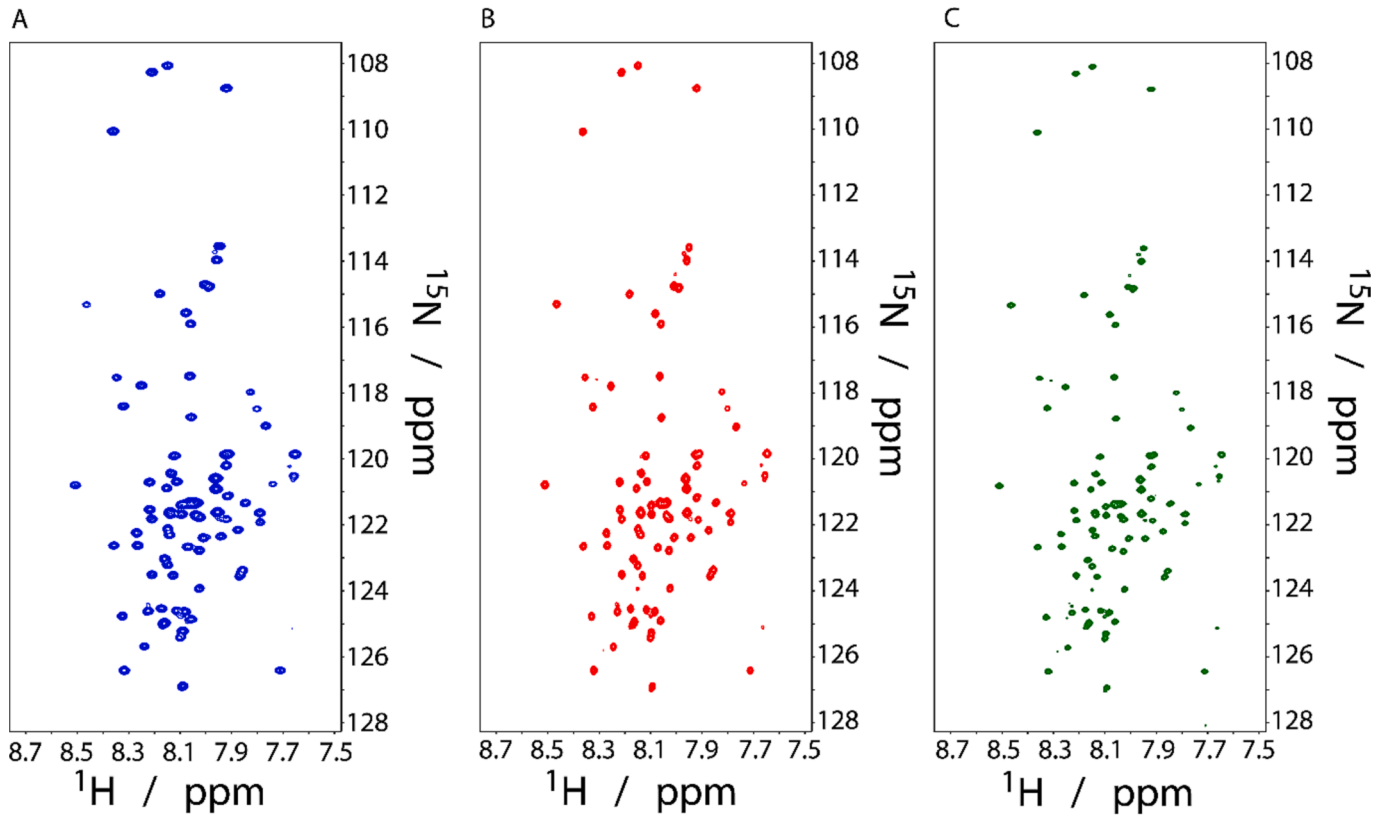

Fig. 2. Two-dimensional ^{1}H-^{15}N HSQC spectra of fully protonated Syb-2 (1–96). All spectra were acquired at 5 °C with 8 scans, an interscan delay of 1.2 s, and a spectral width of 16 ppm in ^{1}H dimension and 30 ppm in ^{15}N dimension. A: HSQC at 600 MHz with 1024 complex points in the ^{1}H dimension and 256 complex points recorded in the ^{15}N dimension. B: HSQC at 1200 MHz with 2048 complex points in the ^{1}H dimension and 256 in the ^{15}N dimension. **C**: HSQC at 1200 MHz with 2048 complex points in the ^{1}H dimension and 512 complex points in the ^{15}N dimension, resulting in the same acquisition time as 600 MHz (but doubling the experimental time).

of improvement is higher than at 600 MHz using a 5 mm Bruker QCI probe. The same sample in a 3 mm NMR tube was used for both NMR spectrometers.

3.3. Protonated sample: Comparison between TROSY- and HSQC-detection scheme

3.3.1. Application at 1200 MHz

The ^{15}N R_1 and $R_{1\rho}$ relaxation rate constants of the fully protonated ^{15}N Syb-2 (1–96) sample measured at 1200 MHz using the sensitivity-enhanced HSQC detection scheme displayed in Fig. 1 are shown in Fig. 4A and 4D (blue) and compared to the data obtained using TROSY-detected pulse sequences (orange) [51]. The ^{15}N R_2 rate constants are derived from the measured ^{15}N R_1 and $R_{1\rho}$ rate constants using the formula (1). Low ^{15}N R_2 rate constants indicate high internal dynamics at the N-terminus of Syb-2 (1–96), consistent with the intrinsically disordered state of monomeric Syb-2. Increasing relaxation rate constants along the protein backbone to the C-terminus point to decreasing internal dynamics. In the region of residue S80 up to W90 the R_2 relaxation rate constants reach a maximum before the rates drop due to the internal highly dynamic amino acids at the C-terminus. These observations correspond well to our earlier finding on $^{2}H^{15}N^{13}C$ Syb-2 (1–96) [57]. The R_1 data only show small variations along the sequence and do not follow a clear trend.

We re-emphasize that the HSQC-detected and the TROSY-detected schemes measure the "standard" R_1 and $R_{1\rho}$ auto-correlation rate constants.

The ^{15}N R_1 rate constants, measured using either the HSQC or the TROSY-detection scheme, follow a very similar pattern and show a high correlation, with a Pearson correlation coefficient of $R = 0.989$ and a root mean square deviation (rmsd) of 0.021 (Fig. 4B). A box plot analysis was performed to assess the agreement quality better. In Fig. 4C, the difference of rate constants is measured using the HSQC or TROSY detection scheme. The agreement is best if the average deviation is zero and the width of the distribution, shown by the box plot bar (interquartile range), is small. We find that the average of the R_1 rate constants measured using the TROSY-detection scheme minus those measured using the HSQC-detection scheme is about −0.76 %. This means that rate constants measured using the TROSY-detection scheme are underestimated compared to those obtained using the HSQC-detection scheme by about 0.76 %. We observe an experimental error between 0.2 % (most intense resonances) and 3 % (least low resonances) for the HSQC-detected and between 0.3 % and 4 % for the TROSY experiment.

The ^{15}N R_2 rate constants (obtained from the ^{15}N $R_{1\rho}$ rate constants by formula 1) are, on average, about −0.84 % lower for the TROSY-detection scheme than for the HSQC-detection scheme (Fig. 4F) but agree with a Pearson correlation coefficient $R = 0.997$ and an rmsd = 0.444. The experimental error is 0.3 % and 3 % for the HSQC-detected experiment and between 0.4 % and 4 % for the TROSY-detected experiments.

Compared to the TROSY-based $R_{1\rho}$ experiment [51], in the new pulse scheme presented in Fig. 1B, we modified the way the evolution of cross-correlated relaxation is refocused. In the new experiment, two 180° I-BURP-2, selective to the amide protons and spaced at Δ*1/4 and Δ*3/4 duration of the relaxation period, refocus the cross-correlated relaxation. Previously, this was achieved by two hard 180° ^{1}H composite pulses. To avoid radiation damping of the water magnetization, a very weak gradient (that alternated its phase halfway) was introduced between those two 180° ^{1}H composite pulses [51]. As evident from Fig. S3,

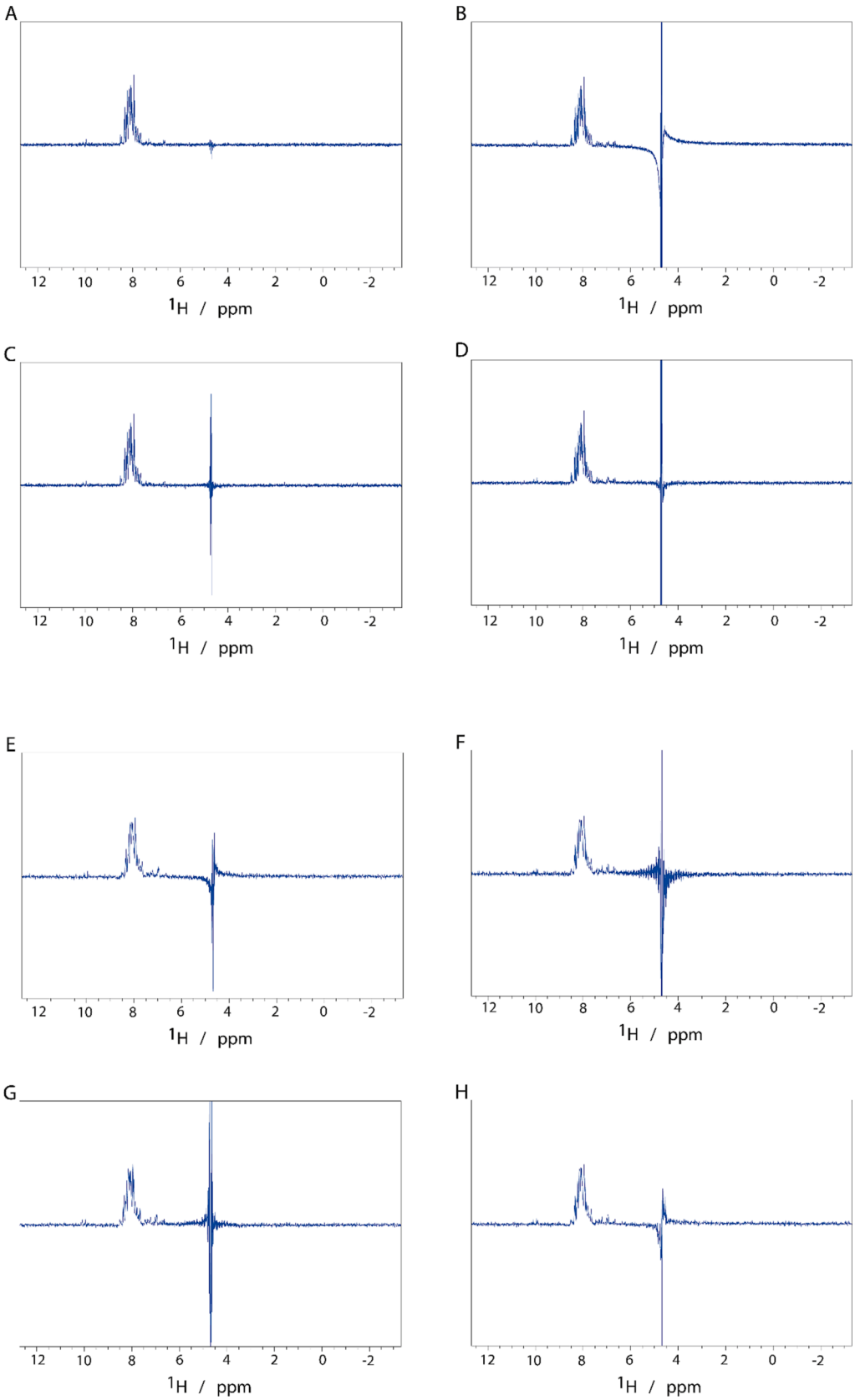

Fig. 3. Improvement of water suppression in ^{15}N $R_{1\rho}$ and $R_{1\rho}$ NMR relaxation experiments with sensitivity-enhanced HSQC-detection using the new implementation (left, see also Fig. 1) and compared to the old implementation (right, SI Fig. S1 in [51]). Shown is the 1D spectrum obtained from the first FID recorded on the protonated ^{15}N Syb-2 sample. (A) Optimized ^{15}N $R_{1\rho}$ experiment at 1200 MHz compared to (B) previous implementation. ^{15}N R_1 experiment at 1200 MHz: (C) new and (D) old. ^{15}N $R_{1\rho}$ experiment at 600 MHz: (E) new and (F) old. ^{15}N R_1 experiment at 600 MHz: (G) new and (H) old.

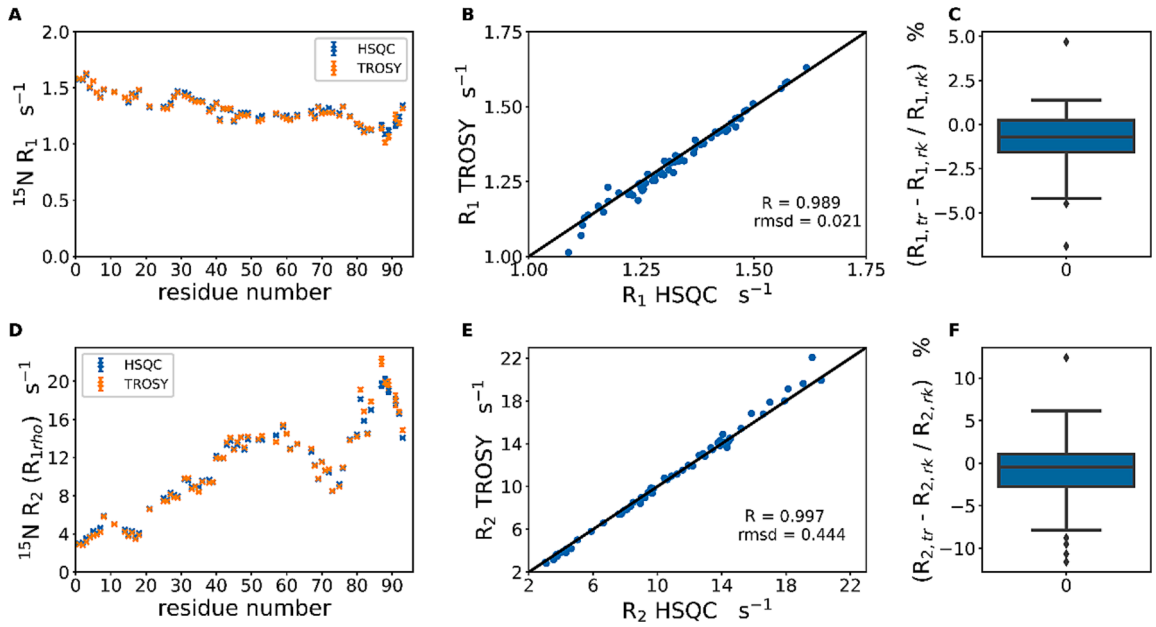

Fig. 4. Comparison of relaxation rates of fully protonated ^{1}H-^{15}N Syb-2 (1–96) acquired with the pulse schemes in Fig. 1 A, B at 1200 MHz and compared to data recorded on the same sample using the TROSY read-out pulse schemes. A: Residue-specific R_1 relaxation rate comparison. B: Correlation plot of the compared R_1 relaxation rate constants. C: Box plot of the residue-specific percentual differences of R_1 relaxation rate constants. D-F: Same plots as in A-C, illustrating the comparison of R_2 ($R_{1\rho}$) rate constants.

we find excellent agreement between relaxation rate constants measured using either of both implementations. In our hand, the new implementation using amide selective I-BURP-2 pulses shows slightly better overall water suppression.

The 2 kHz spinlock RF amplitude used at 1200 MHz seems sufficient to avoid off-resonance effects. At least we do not observe any unexpected deviations of the ^{15}N R_2 rate constants of residues with the most ^{15}N upfield or downfield resonances (Fig. S4).

3.3.2. Application at 600 MHz

To test the applicability of the pulse sequences with sensitivity-enhanced HSQC detection on a 600 MHz spectrometer, we recorded ^{15}N R_1 and ^{15}N $R_{1\rho}$ experiments on the protonated sample, using either the HSQC or the original TROSY-detection scheme. Also, at 600 MHz, the ^{15}N R_1 rate constants show good agreement (Fig. 5A-C), with a Pearson correlation coefficient of R = 0.949 and a rmsd of 0.032 (Fig. 5B). For the box plot analysis, the average deviation between both data sets is −0.45 % and a relatively even distribution around that is observed (Fig. 5C), pointing to a stochastic experimental error.

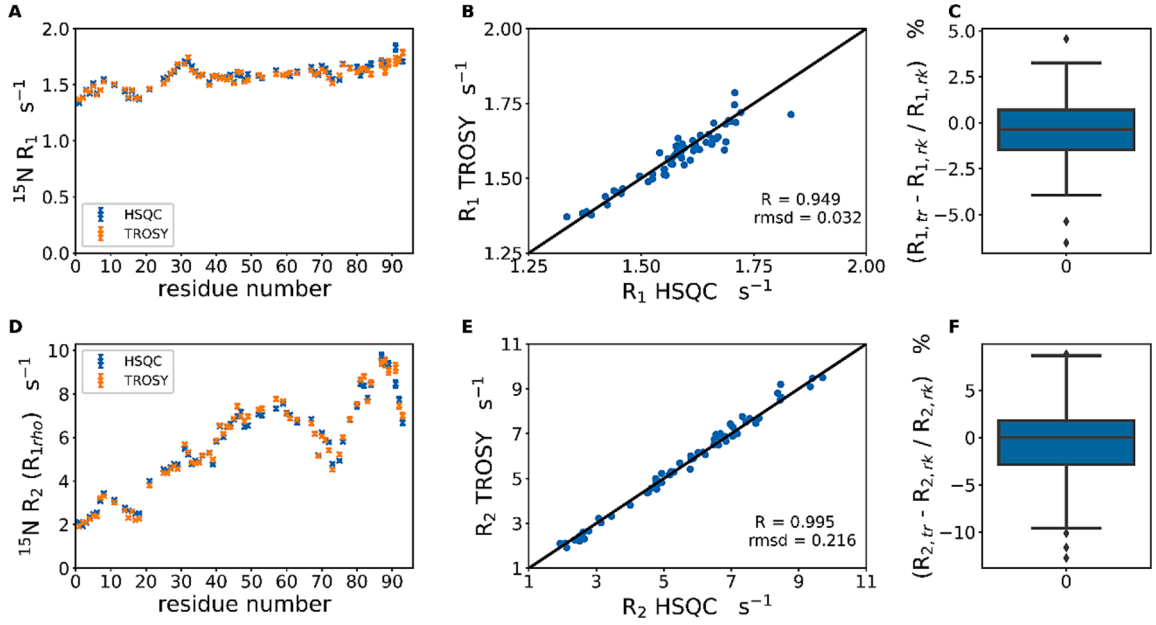

Fig. 5. Comparison of relaxation rate constants of protonated ^{15}N Syb-2 (1–96) at 600 MHz, acquired with the pulse schemes in Fig. 1 A, B, using sensitivity-enhanced HSQC detection and, for comparison, with the TROSY-detection. A: Residue-specific R_1 relaxation rate constants comparison. B: correlation plot of the R_1 relaxation rate constants. C: Box plot of the residue-specific percentual differences of R_1 relaxation rates. D-F: Same plots as in A-C, illustrating the comparison of R_2 ($R_{1\rho}$) rate constants.

The ^{15}N R_2 rate constants, derived from the ^{15}N $R_{1\rho}$ rate constants by formula 1, show good agreement with a Pearson correlation coefficient of R = 0.995 and a rmsd of 0.216 (Fig. 5E). ^{15}N R_2 data obtained using the TROSY-detection scheme are, on average −0.43 % lower than the ones obtained using the sensitivity-enhanced HSQC-detection scheme. For both experiments the average deviation lies within the experimental error margin (between 0.5 % and 2 % for HSQC and 0.5 % and 3 % for TROSY).

3.3.3. Signal-to-noise comparison

TROSY-detection schemes offer several advantages, such as excellent water suppression (see above) due to fewer pulses and the absence of proton decoupling. Also, in terms of line widths, TROSY-detection will yield smaller line widths and, therefore, better resolution compared to HSQC-detection because of the partial cancellation of the transverse auto-relaxation and cross-correlated relaxation, resulting in slower transverse relaxation and in turn reduced line widths. In addition, in principle, longer acquisition times in the direct dimension can be afforded due to the absence of composite pulse decoupling during the acquisition period, so resolution is not limited by the acquisition time. For higher molecular weight proteins (>20 kDa), TROSY will also win over HSQC regarding signal-to-noise.

However, for small and medium-sized proteins, in particular, at low concentrations, the sensitivity-enhanced detection scheme offers a higher signal-to-noise ratio (SNR). Table 1 shows a signal-to-noise comparison between the HSQC and TROSY-detection schemes. For fully protonated Syb-2, which is an IDP, we find an approximately two-fold increase in the SNR when using the sensitivity-enhanced HSQC scheme compared to the TROSY-detection scheme, which agrees with the maximum theoretically expected improvement of the HSQC vs TROSY-detection (which is two-fold), based on detection of the H^- operator of the sensitivity-enhanced HSQC detection compared to detection of the H^-N^β operator for (sensitivity-enhanced) TROSY detection. However, we also find slower ^{1}H T_1 relaxation of the H^-N^β TROSY line used for detection than the H^- operator in the HSQC scheme (see Fig. S5). We estimated ^{1}H T_1 (TROSY) = 1.24 s, compared to ^{1}H T_1 (HSQC) = 0.86 s at 1200 MHz, which further enhances the SNR in the HSQC-detection scheme, given the inter-scan recovery delay of 2 s, used in both experiments.

3.4. Relaxation rate constants of deuterated vs. protonated ^{15}N Syb-2 (1–96)

3.4.1. ^{15}N R_1 experiment

Figs. 4 and 5 show the rate constants measured on a fully protonated ^{15}N Syb-2 (1–96) sample. In principle, the N-H amide group can be considered an isolated two-spin system in good approximation. However, we cannot exclude a residual interaction with the surrounding proton network. Therefore, measuring relaxation rate constants on a deuterated sample, with aliphatic side chains deuterated, and amide protons and exchangeable side-chain protons fully back-exchanged to protons (in a protonated buffer) is preferable in principle [79–81]. However, deuteration is cost-extensive, and frequently, deuteration puts an additional burden on the biochemical sample preparation. We, therefore, tested how well the rate constants agree for a fully protonated versus a deuterated sample, with amide protons fully back-exchanged (Fig. 6).

Fig. 6A shows a residue-wise comparison of the measured ^{15}N R_1 rate constants of the fully protonated ^{15}N Syb-2 (1–96) sample (compare Fig. 4A) with those measured on the deuterated ^{2}H^{15}N Syb-2 (1–96) sample (of equal concentration). Both samples were measured using the sensitivity-enhanced HSQC-detection scheme. On both samples, the ^{15}N R_1 rate constants follow a very similar pattern and show a high correlation, with a Pearson correlation coefficient of R = 0.976 and a root mean square deviation (rmsd) of 0.026 (Fig. 6B). In Fig. 6C, the difference in rate constants is measured on the protonated and deuterated samples. We find that the average deviation of the R_1 rate constants measured on the protonated sample minus those on the deuterated sample is close to zero on average.

For deuterated samples, ^{1}H T_1 times increase because of the more dilute proton network. We, therefore, compared different interscan recovery delays (2 s vs. 4 s). Fig. S6 compares the ^{15}N R_1 experiment (Fig. 1A), recorded with a 2 s vs 4 s interscan recovery delay, both for the fully protonated (Fig. S6 A-C) and the deuterated sample (Fig. S6 D-F). The 2 s and the 4 s experiment correlate with R = 0.992 (protonated) and R = 0.985 (deuterated), and a rmsd of 0.016 and 0.02, respectively, indicating high correspondence between both experiments (2 s vs. 4 s interscan recovery delay). Also, data points scatter stochastically, and the average difference is close to zero. Thus, we concluded that a 2 s

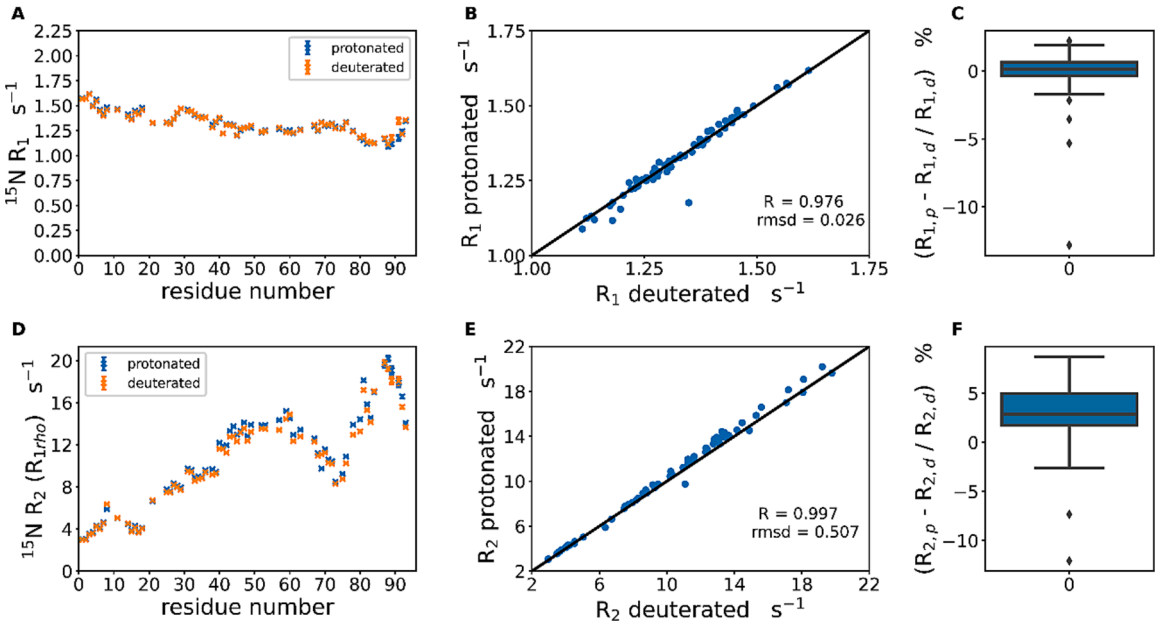

Fig. 6. Comparison of relaxation rate constants of deuterated ^{2}H-^{15}N Syb-2 (1–96) and protonated ^{1}H-^{15}N Syb-2 (1–96) acquired with the pulse schemes in Fig. 1 A, B at 1200 MHz. A: Residue-specific comparison of ^{15}N R_1 relaxation rate constants. B: Correlation plot of the compared R_1 relaxation rate constants. C: Box plot of the residue-specific percentual differences of R_1 relaxation rate constants. D-F: Same comparing plots as in A-C, but illustrating the comparison of R_2 ($R_{1\rho}$) rate constants.

interscan delay is sufficient.

A modified ^{15}N R_1 relaxation experiment has been suggested [82], which maintains the transverse magnetization of aliphatic protons in a dephased state (saturated state) during the variable ^{15}N relaxation period T and uses a cosine modulated I-BURP-2 scheme that inverts both the amide and the aliphatic protons simultaneously. In our hands, ^{15}N R_1 data recorded on the fully protonated sample agree well with those on the deuterated sample, arguing against a strong impact of the magnetization state of the aliphatic protons.

3.4.2. ^{15}N $R_{1\rho}$ experiment

Fig. 6D compares the ^{15}N R_2 rate constants measured using the HSQC vs the TROSY detection scheme. While we find a Pearson correlation coefficient of R = 0.997 and rmsd of 0.507 (Fig. 6E), indicating a close correlation, we also observe an offset of, on average, 2.79 % higher values observed for the protonated sample (Fig. 6F). More structure/rigid residues show a more substantial deviation.

Deuteration of protein side chains may have a minimal impact on protein dynamics [83], e.g., the C-D bond length is marginally shorter than the C-H bond lengths (approx. 0.005 Å) [84]. However, this impact is subtle and less clear than dissolving the protein in a buffer of heavy water (D_2O) [83,85]. Here, we work with a deuterated protein dissolved in H_2O buffer (with only 5 % D_2O added for reference). The slightly reduced C-D bond lengths may lead to an overall marginally smaller hydrodynamic radius, affecting the overall tumbling correlation time. This may explain the slightly lower ^{15}N R_2 rate constants observed for the deuterated sample.

3.5. Deuterated sample: Comparison between TROSY- and HSQC-detection scheme

To test whether, for the deuterated Syb-2 sample, the TROSY-detection scheme yields the same rate constants as when using a sensitivity-enhanced HSQC read-out scheme, we repeated the analysis described in section 3.3. (protonated sample) also for the deuterated sample.

3.5.1. Application at 1200 MHz

Fig. 7 compares the ^{15}N R_1 and $R_{1\rho}$ experiments recorded with the TROSY-detection scheme and the sensitivity-enhanced HSQC-detection scheme. Data were recorded at 1200 MHz. In Fig. 7A, both R_1 data sets show only minor, non-systematic differences and follow a similar pattern. The correlation plot also shows a strong correlation between both data sets (Fig. 7B). As demonstrated in the box plot in Fig. 7C, ^{15}N R_1, and R_2 rate constants are, on average, 0.59 % and 0.80 % higher for the HSQC-detected experiments vs. the TROSY-detected ones. An even stronger correlation between both pulse schemes is observed for the R_2 datasets (Fig. 7 D-F), underlined by a correlation coefficient R = 0.997 and rmsd of 0.359.

3.5.2. Application at 600 MHz

We also recorded the ^{15}N R_1 and ^{15}N $R_{1\rho}$ experiments with sensitivity-enhanced HSQC detection and, for comparison with TROSY-detection at 600 MHz spectrometer, using the deuterated sample. Also, at 600 MHz, the ^{15}N R_1 rate constants show good agreement (Fig. 8A-C), with a Pearson correlation coefficient of R = 0.955 and a rmsd of 0.031 (Fig. 8B). For the box plot analysis, a close to zero average deviation between both data sets and a relatively even distribution around that is observed (Fig. 8C), pointing to a stochastic experimental error.

The ^{15}N R_2 rate constants, derived from the ^{15}N $R_{1\rho}$ rate constants by formula 1, show good agreement with a Pearson correlation coefficient of R = 0.994 and a rmsd of 0.214 (Fig. 8E) and close to zero average deviation.

4. Conclusions

Advances in magnet technology have led to higher available field strengths, which have improved spectral resolution. Hence, new opportunities are offered, especially regarding the investigations of IDPs.

Recently, NMR relaxation measurements could provide novel insights into fast internal protein dynamics of intrinsically disordered proteins [19–21,86–99]. Temperature-dependent NMR relaxation experiments have allowed for identifying different dynamics modes in an intrinsically disordered protein [87,89] or examining the effect of crowding on IDP dynamics [13,86,98]. Detailed atomic-resolution

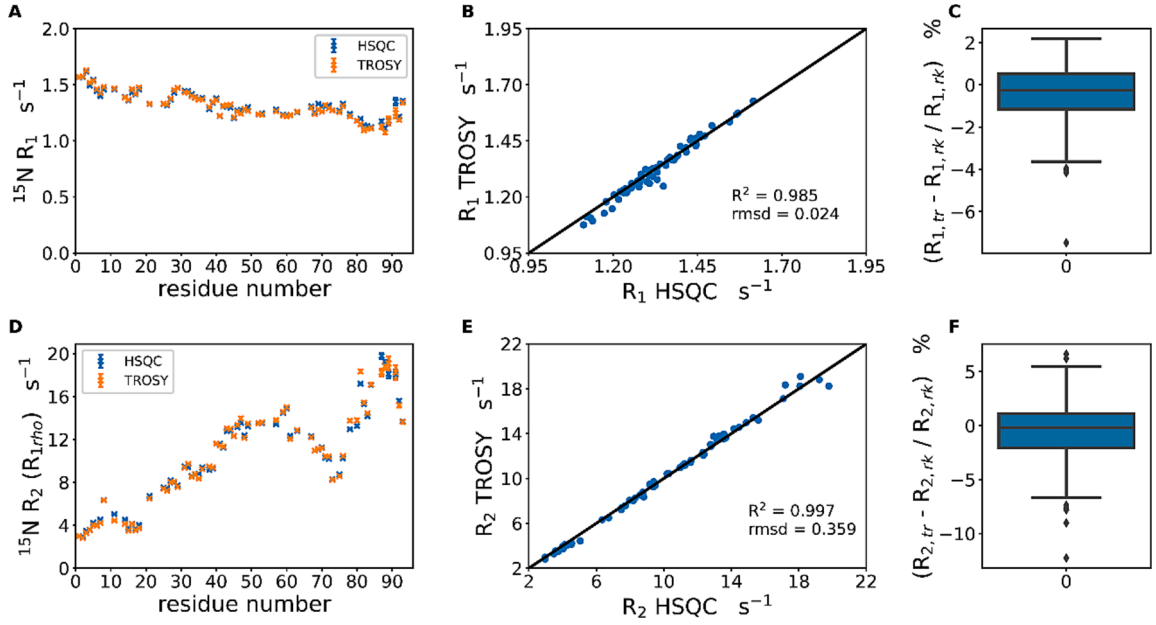

Fig. 7. Comparison of relaxation rates of deuterated ^{2}H-^{15}N Syb-2 (1–96) acquired with the pulse schemes in Fig. 1 A, B at 1200 MHz and of deuterated ^{2}H-^{15}N Syb-2 (1–96) obtained with the TROSY read-out schemes [51] at 1200 MHz. A: Residue-specific R_1 relaxation rate comparison. B: Correlation plot of the compared R_1 relaxation rate constants. C: Box plot of the residue-specific percentual differences of R_1 relaxation rate constants. D-F: Same plots as in A-C, but illustrating the R_2 ($R_{1\rho}$) rates comparison.

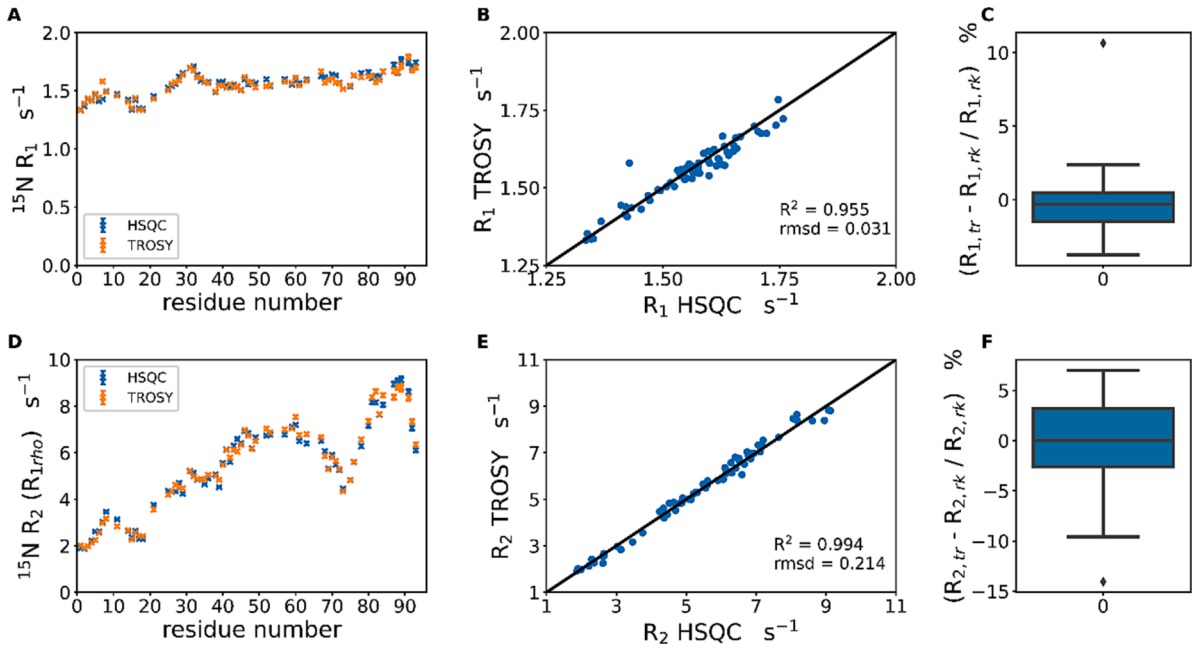

Fig. 8. Comparison of relaxation rates of deuterated ^{2}H-^{15}N Syb-2 (1–96) acquired with the pulse schemes in Fig. 1 A, B at 600 MHz and of deuterated ^{2}H-^{15}N Syb-2 (1–96) obtained with the TROSY read-out schemes [51] at 600 MHz. A: Residue-specific R_1 relaxation rate comparison. B: Correlation plot of the compared R_1 relaxation rate constants. C: Box plot of the residue-specific percentual differences of R_1 relaxation rate constants. D-F: Same plots as in A-C, but illustrating the R_2 ($R_{1\rho}$) rates comparison.

insights on IDP dynamics can be obtained when NMR relaxation measurements are combined with molecular dynamics simulations [88,100] or further experimental probes, such as e.g. fluorescence or SAXS measurements, are included [101–103].

We established sensitivity-enhanced HSQC-based R_1 and $R_{1\rho}$ relaxation pulse sequences with improved water suppression and tested them at 14.1 T (600 MHz ^{1}H Larmor frequency) and 28 T (1200 MHz ^{1}H Larmor frequency). We showed that relaxation rate constants obtained using these pulse sequences correspond well with those obtained using the TROSY-based pulse schemes introduced previously [51]. These pulse schemes reduce systematic errors from partial water saturation and cross-correlated relaxation. As we observe high robustness and reproducibility of the ^{15}N R_1 and $R_{1\rho}$ experiments both at 600 MHz and 1200 MHz, we conclude that both the sensitivity-enhanced HSQC-detected experiments as well as the TROSY-detected experiments can be applied for any magnetic field in between, ranging between 600 MHz and 1200 MHz.

Further, we showed a high correlation and high agreement of relaxation rate constants between a deuterated and non-deuterated protein sample, using both sets of pulse sequences (sensitivity-enhanced HSQC and TROSY-based). Our data demonstrate that reliable relaxation rate constants can be obtained on fully protonated samples, and deuteration (for getting isolated ^{1}H-^{15}N spin pairs) is not required per se. Consequently, the subset of proteins accessible to a backbone structural dynamic investigation is enlarged, simultaneously reducing the costs of NMR sample preparation. The presented NMR relaxation sequences sensitivity-enhanced HSQC-detected are not limited to IDPs but will work equally well for small and medium-sized proteins.

4.1. Which detection scheme to use? TROSY or HSQC?

The $H^{-}N^{\beta}$ TROSY-line detected in the TROSY-based read-out scheme shows slower relaxation (and sharper linewidth) than the H^{-} line detected in the sensitivity-enhanced HSQC experiments. (The H^{-} operator results from applying the H^{+} detection operator on the H_x or H_y operator, respectively.) The slower relaxation of the TROSY line originates from the partial cancellation of the R_2 auto-relaxation and the transverse cross-correlated relaxation of N-H dipolar coupling and the ^{15}N chemical shift anisotropy [69]. This partial cancellation becomes effective at ^{1}H Larmor frequencies above 500 MHz and reaches a maximum of around 1000 MHz [104,105]. The corresponding line widths will also be smaller because of the TROSY line's slower relaxation. Therefore, TROSY detection is always preferable in terms of line width. However, as only one doublet component is detected, the signal intensity will only be half if relaxation is neglected. Therefore, for a small and highly dynamic protein (which is characterized by small transverse relaxation rate constants), such as the IDP investigated here, the HSQC signal intensity will be twice, as both the $H^{-}N^{\beta}$ and $H^{-}N^{\alpha}$ line will add up and be detected in the decoupled HSQC spectra.

The resulting signal intensity, HSQC vs TROSY, will now be a trade-off between the double signal intensity of the HSQC spectra (in the absence of relaxation) and the TROSY line ($H^{-}N^{\beta}$ in the direct ^{1}H dimension and $N^{-}H^{\beta}$ in the indirect ^{15}N dimension, respectively) becoming gradually stronger for increased transverse relaxation. At some point, the intensity of the TROSY line will become more intense than the HSQC line (which is the average of the TROSY and anti-TROSY line because of $H^{-}N^{\beta} + H^{-}N^{\alpha} = 2H^{-}$). This is the breakeven that will be reached when TROSY outperforms HSQC, not only in terms of line width but also in terms of SNR. For a fully protonated rigid globular folded protein, the breakeven will be reached at a molecular weight (MW) of about 20–30 kDa. For even higher MWs, deuteration of the protein is recommended to dilute the proton network and reduce transverse relaxation due to ^{1}H–^{1}H dipolar couplings with the surrounding proton network. This breakeven for proteins with high internal dynamics will be shifted towards higher MWs as fast internal dynamics will lead to lower transverse relaxation rates.

In the following, we will give a brief guideline on when to choose the TROSY and when to select the sensitivity-enhanced HSQC detected ^{15}N R_1 and ^{15}N $R_{1\rho}$ experiments:

1. When the main priority is to obtain the highest resolution (smallest line widths), the TROSY-detected experiments will always be the best option.

2. TROSY-detected experiments will also always give the best water suppression.
3. When a high signal-to-noise ratio (SNR) is the main criterion, it will be a judgment call, depending on the following points: (A) The molecular weight of the investigated biomolecule, (B) the (expected) internal dynamics of the studied biomolecule, (C) the magnetic field the sample is measured at, and (D) whether a fully protonated or a deuterated sample is used.

(A) Below 20 kDa, we recommend using the sensitivity-enhanced HSQC detection when SNR is the main criterion.
(B) Proteins with high internal dynamics (like IDPs) will give more intense resonances due to smaller transverse relaxation. Therefore, for IDPs, the HSQC detection may be beneficial up to 30 kDa.
(C) Below 800 MHz, the TROSY effect will be less effective. Therefore, the breakeven point for TROSY may be shifted towards higher MW.
(D) The TROSY effect will be more effective for deuterated proteins, shifting the breakeven points to lower MW.

This brief guideline can, however, only be over-simplified because all factors A to D contribute and will influence each other. Therefore, we strongly recommend to follow the following empirical approach:

TROSY will always win in terms of line width. If SNR is the main criterion, we suggest the following approach:

1. Set up both the TROSY-detected and the HSQC-detected NMR relaxation experiments. (With the easier-to-optimize HSQC-detected NMR experiments, this should be easy.)
2. Record the first FID of each sequence. The corresponding 1D spectrum (after the Fourier-Transformation of the first FID) will yield a good impression of the expected SNR. Choose the detection scheme that offers higher SNR.
3. To estimate the maximum duration that should be sampled, record, e.g., the second FID with the most extended relaxation delay period. If possible, the entire exponential decay curve down to 30 % of the initial signal intensity should be sampled.
4. For the ^{15}N $R_{1\rho}$ experiment, be careful not to exceed the (probe and spectrometer-specific) maximum power and duration of the CW irradiation during the spinlock period of the relaxation delay.

5. Funding Source

Heisenberg Program (DFG grant number 433700474) “Virological and immunological determinants of COVID-19 pathogenesis – lessons to get prepared for future pandemics (KA1-Co-02 “COVIPA”)”, a grant from the Helmholtz Association’s Initiative and Networking Fund.

CRediT authorship contribution statement

Tobias Stief: Investigation, Methodology, Formal analysis, Writing – original draft, Writing – review & editing. **Katharina Vormann:** Resources, Writing – original draft, Writing – review & editing. **Nils-Alexander Lakomek:** Conceptualization, Methodology, Supervision, Funding acquisition, Writing – original draft, Writing – review & editing.

Declaration of competing interest

The authors declare that they have no known competing financial interests or personal relationships that could have appeared to influence the work reported in this paper.

Data availability

Data will be made available on request.

Acknowledgments

We thank Robin Backer, Lothar Gremer, Filip Hasecke, Nina Kirchgässler, Anne Pfitzer, Celina M. Schulz, Nasrollah Rezaei-Ghaleh, and Marie Schützmann for helpful discussions. N.L. thanks the German Science Foundation for funding through the Heisenberg Program (DFG grant number 433700474). This work is further supported by the project “Virological and immunological determinants of COVID-19 pathogenesis – lessons to get prepared for future pandemics (KA1-Co-02 “COVIPA”), a grant from the Helmholtz Association’s Initiative and Networking Fund. We acknowledge generous access to the Jülich-Düsseldorf Biomolecular NMR Center, jointly run by Forschungszentrum Jülich and Heinrich Heine University Düsseldorf (HHU).

Appendix A. Supplementary data

Supplementary data (Experimental details on the NMR experiments, supplementary NMR data, and ^{15}N R_1 and $R_{1\rho}$ rate constants) to this article can be found online at https://doi.org/10.1016/j.ymeth.2024.01.008.

References

[1] P. Tompa, Intrinsically unstructured proteins, Trends Biochem. Sci 27 (10) (2002) 527–533.
[2] V.N. Uversky, Natively unfolded proteins: a point where biology waits for physics, Protein Sci. 11 (4) (2002) 739–756.
[3] H.J. Dyson, P.E. Wright, Intrinsically unstructured proteins and their functions, Nat. Rev. Mol. Cell Biol. 6 (3) (2005) 197–208.
[4] P.E. Wright, H.J. Dyson, Intrinsically disordered proteins in cellular signalling and regulation, Nat. Rev. Mol. Cell Biol. 16 (1) (2015) 18–29.
[5] K. Sugase, H.J. Dyson, P.E. Wright, Mechanism of coupled folding and binding of an intrinsically disordered protein, Nature 447 (7147) (2007) 1021–1025.
[6] T. Mittag, J.D. Forman-Kay, Atomic-level characterization of disordered protein ensembles, Curr. Opin. Struct. Biol. 17 (1) (2007) 3–14.
[7] A. Bah, R.M. Vernon, Z. Siddiqui, M. Krzeminski, R. Muhandiram, C. Zhao, N. Sonenberg, L.E. Kay, J.D. Forman-Kay, Folding of an intrinsically disordered protein by phosphorylation as a regulatory switch, Nature 519 (7541) (2015) 106–109.
[8] K.A. Burke, A.M. Janke, C.L. Rhine, N.L. Fawzi, Residue-by-residue view of in vitro FUS granules that bind the C-terminal domain of RNA polymerase II, Mol. Cell 60 (2) (2015) 231–241.
[9] T.J. Nott, E. Petsalaki, P. Farber, D. Jervis, E. Fussner, A. Plochowietz, T. D. Craggs, D.P. Bazett-Jones, T. Pawson, J.D. Forman-Kay, A.J. Baldwin, Phase transition of a disordered nuage protein generates environmentally responsive membraneless organelles, Mol. Cell 57 (5) (2015) 936–947.
[10] C.W. Pak, M. Kosno, A.S. Holehouse, S.B. Padrick, A. Mittal, R. Ali, A.A. Yunus, D. R. Liu, R.V. Pappu, M.K. Rosen, Sequence determinants of intracellular phase separation by complex coacervation of a disordered protein, Mol. Cell 63 (1) (2016) 72–85.
[11] S. Boeynaems, S. Alberti, N.L. Fawzi, T. Mittag, M. Polymenidou, F. Rousseau, J. Schymkowitz, J. Shorter, B. Wolozin, L. Van den Bosch, P. Tompa, M. Fuxreiter, Protein phase separation: A new phase in cell biology, Trends Cell Biol. 28 (6) (2018) 420–435.
[12] M. Boehning, C. Dugast-Darzacq, M. Rankovic, A.S. Hansen, T. Yu, H. Marie-Nelly, D.T. McSwiggen, G. Kokic, G.M. Dailey, P. Cramer, X. Darzacq, M. Zweckstetter, RNA polymerase II clustering through carboxy-terminal domain phase separation, Nat. Struct. Mol. Biol. 25 (9) (2018) 833–840.
[13] S. Guseva, V. Schnapka, W. Adamski, D. Maurin, R.W.H. Ruigrok, N. Salvi, M. Blackledge, Liquid-liquid phase separation modifies the dynamic properties of intrinsically disordered proteins, J. Am. Chem. Soc. 145 (19) (2023) 10548–10563.
[14] C.M. Dobson, Protein folding and misfolding, Nature 426 (6968) (2003) 884–890.
[15] C.W. Bertoncini, Y.S. Jung, C.O. Fernandez, W. Hoyer, C. Griesinger, T.M. Jovin, M. Zweckstetter, Release of long-range tertiary interactions potentiates aggregation of natively unstructured alpha-synuclein, Proc. Natl. Acad. Sci. U. S. A. 102 (5) (2005) 1430–1435.
[16] A.K. Buell, C. Galvagnion, R. Gaspar, E. Sparr, M. Vendruscolo, T.P. Knowles, S. Linse, C.M. Dobson, Solution conditions determine the relative importance of nucleation and growth processes in alpha-synuclein aggregation, Proc. Natl. Acad. Sci. U. S. A. 111 (21) (2014) 7671–7676.
[17] A. Patel, H.O. Lee, L. Jawerth, S. Maharana, M. Jahnel, M.Y. Hein, S. Stoynov, J. Mahamid, S. Saha, T.M. Franzmann, A. Pozniakovski, I. Poser, N. Maghelli, L. A. Royer, M. Weigert, E.W. Myers, S. Grill, D. Drechsel, A.A. Hyman, S. Alberti, A liquid-to-solid phase transition of the ALS protein FUS accelerated by disease mutation, Cell 162 (5) (2015) 1066–1077.
[18] M.R. Jensen, L. Salmon, G. Nodet, M. Blackledge, Defining conformational ensembles of intrinsically disordered and partially folded proteins directly from chemical shifts, J. Am. Chem. Soc. 132 (4) (2010) 1270–1272.

[19] A.R. Camacho-Zarco, V. Schnapka, S. Guseva, A. Abyzov, W. Adamski, S. Milles, M.R. Jensen, L. Zidek, N. Salvi, M. Blackledge, NMR provides unique insight into the functional dynamics and interactions of intrinsically disordered proteins, Chem. Rev. 122 (10) (2022) 9331–9356.
[20] N. Rezaei-Ghaleh, G. Parigi, A. Soranno, A. Holla, S. Becker, B. Schuler, C. Luchinat, M. Zweckstetter, Local and global dynamics in intrinsically disordered synuclein, Angew. Chem. Int. Ed. Engl. 57 (46) (2018) 15262–15266.
[21] R. Schneider, M. Blackledge, M.R. Jensen, Elucidating binding mechanisms and dynamics of intrinsically disordered protein complexes using NMR spectroscopy, Curr. Opin. Struct. Biol. 54 (2019) 10–18.
[22] T.R. Alderson, L.E. Kay, NMR spectroscopy captures the essential role of dynamics in regulating biomolecular function, Cell 184 (3) (2021) 577–595.
[23] L.E. Kay, D.A. Torchia, A. Bax, Backbone dynamics of proteins as studied by 15N inverse detected heteronuclear NMR spectroscopy: application to staphylococcal nuclease, Biochemistry 28 (23) (1989) 8972–8979.
[24] J.W. Peng, G. Wagner, Mapping of the spectral densities of N-H bond motions in eglin c using heteronuclear relaxation experiments, Biochemistry 31 (36) (1992) 8571–8586.
[25] N.A. Farrow, R. Muhandiram, A.U. Singer, S.M. Pascal, C.M. Kay, G. Gish, S. E. Shoelson, T. Pawson, J.D. Formankay, L.E. Kay, Backbone dynamics of a free and a phosphopeptide-complexed SRC homology-2 domain studied by N-15 NMR relaxation, Biochemistry 33 (19) (1994) 5984–6003.
[26] G. Barbato, M. Ikura, L.E. Kay, R.W. Pastor, A. Bax, Backbone dynamics of Calmodulin studied by N-15 relaxation using inverse detected 2-dimensional NMR-spectroscopy - The central helix is flexible, Biochemistry 31 (23) (1992) 5269–5278.
[27] L.E. Kay, P. Keifer, T. Saarinen, Pure Absorption Gradient enhanced heteronuclear single quantum correlation spectroscopy with improved sensitivity, J. Am. Chem. Soc. 114 (26) (1992) 10663–10665.
[28] L.E. Kay, Protein dynamics from NMR, Nat. Struct. Biol. 5 (1998) 513–517.
[29] R. Ishima, D.A. Torchia, Protein dynamics from NMR, Nat. Struct. Biol. 7 (9) (2000) 740–743.
[30] S.F. Lienin, T. Bremi, B. Brutscher, R. Bruschweiler, R.R. Ernst, Anisotropic intramolecular backbone dynamics of ubiquitin characterized by NMR relaxation and MD computer simulation, J. Am. Chem. Soc. 120 (38) (1998) 9870–9879.
[31] M. Akke, A.G. Palmer, Monitoring macromolecular motions on microsecond to millisecond time scales by R(1)rho-R(1) constant relaxation time NMR spectroscopy, J. Am. Chem. Soc. 118 (4) (1996) 911–912.
[32] J.P. Loria, M. Rance, A.G. Palmer, A relaxation-compensated Carr-Purcell-Meiboom-Gill sequence for characterizing chemical exchange by NMR spectroscopy, J. Am. Chem. Soc. 121 (10) (1999) 2331–2332.
[33] M. Tollinger, N.R. Skrynnikov, F.A.A. Mulder, J.D. Forman-Kay, L.E. Kay, Slow dynamics in folded and unfolded states of an SH3 domain, J. Am. Chem. Soc. 123 (46) (2001) 11341–11352.
[34] F.A.A. Mulder, N.R. Skrynnikov, B. Hon, F.W. Dahlquist, L.E. Kay, Measurement of slow (mu s-ms) time scale dynamics in protein side chains by N-15 relaxation dispersion NMR spectroscopy: Application to Asn and Gln residues in a cavity mutant of T4 lysozyme, J. Am. Chem. Soc. 123 (5) (2001) 967–975.
[35] D.F. Hansen, P. Vallurupalli, L.E. Kay, An improved (15)N relaxation dispersion experiment for the measurement of millisecond time-scale dynamics in proteins, J. Phys. Chem. B 112 (19) (2008) 5898–5904.
[36] A.G. Palmer, NMR characterization of the dynamics of biomacromolecules, Chem. Rev. 104 (8) (2004) 3623–3640.
[37] A. Mittermaier, L.E. Kay, Review - New tools provide new insights in NMR studies of protein dynamics, Science 312 (5771) (2006) 224–228.
[38] D.D. Boehr, D. McElheny, H.J. Dyson, P.E. Wright, The dynamic energy landscape of dihydrofolate reductase catalysis, Science 313 (5793) (2006) 1638–1642.
[39] K. Henzler-Wildman, D. Kern, Dynamic personalities of proteins, Nature 450 (7172) (2007) 964–972.
[40] P. Neudecker, P. Robustelli, A. Cavalli, P. Walsh, P. Lundstrom, A. Zarrine-Afsar, S. Sharpe, M. Vendruscolo, L.E. Kay, Structure of an intermediate state in protein folding and aggregation, Science 336 (6079) (2012) 362–366.
[41] E.A. Morrison, G.T. DeKoster, S. Dutta, R. Vafabakhsh, M.W. Clarkson, A. Bahl, D. Kern, T. Ha, K.A. Henzler-Wildman, Antiparallel EmrE exports drugs by exchanging between asymmetric structures, Nature 481 (7379) (2012) 45–U50.
[42] J.B. Stiller, R. Otten, D. Haussinger, P.S. Rieder, D.L. Theobald, D. Kern, Structure determination of high-energy states in a dynamic protein ensemble, Nature 603 (7901) (2022) 528-+.
[43] Q. Zhang, X.Y. Sun, E.D. Watt, H.M. Al-Hashimi, Resolving the motional modes that code for RNA adaptation, Science 311 (5761) (2006) 653–656.
[44] I.J. Kimsey, K. Petzold, B. Sathyamoorthy, Z.W. Stein, H.M. Al-Hashimi, Visualizing transient Watson-Crick-like mispairs in DNA and RNA duplexes, Nature 519 (7543) (2015) 315-+.
[45] J. Rinnenthal, J. Buck, J. Ferner, A. Wacker, B. Furtig, H. Schwalbe, Mapping the landscape of RNA dynamics with NMR spectroscopy, Acc. Chem. Res. 44 (12) (2011) 1292–1301.
[46] J. Boyd, U. Hommel, I.D. Campbell, Influence of cross-correlation between dipolar and anisotropic chemical-shift relaxation mechanisms upon longitudinal relaxation rates of N-15 in macromolecules, Chem. Phys. Lett. 175 (5) (1990) 477–482.
[47] L.E. Kay, L.K. Nicholson, F. Delaglio, A. Bax, D.A. Torchia, Pulse sequences for removal of the effects of cross-correlation between dipolar and chemical-shift anisotropy relaxation mechanism on the measurement of heteronuclear T1 and T2 values in proteins, J. Magn. Reson. 97 (2) (1992) 359–375.
[48] A.G. Palmer, N.J. Skelton, W.J. Chazin, P.E. Wright, M. Rance, Suppression of the effects of cross-correlation between dipolar and anisotropic chemical-shift relaxation mechanisms in the measurement of spin spin relaxation rates, Mol. Phys. 75 (3) (1992) 699–711.
[49] S. Grzesiek, A. Bax, The importance of not saturating H2O in protein NMR - Application to sensitivity enhancement and NOE measurements, J. Am. Chem. Soc. 115 (26) (1993) 12593–12594.
[50] K. Chen, N. Tjandra, Water proton spin saturation affects measured protein backbone 15N spin relaxation rates, J. Magn. Reson. 213 (1) (2011) 151–157.
[51] N.A. Lakomek, J. Ying, A. Bax, Measurement of (1)(5)N relaxation rates in perdeuterated proteins by TROSY-based methods, J. Biomol. NMR 53 (3) (2012) 209–221.
[52] R. Ishima, A probe to monitor performance of (1)(5)N longitudinal relaxation experiments for proteins in solution, J. Biomol. NMR 58 (2) (2014) 113–122.
[53] T. Yuwen, N.R. Skrynnikov, Proton-decoupled CPMG: a better experiment for measuring (15)N R2 relaxation in disordered proteins, J. Magn. Reson. 241 (2014) 155–169.
[54] P. Wikus, W. Frantz, R. Kummerle, P. Vonlanthen, Commercial gigahertz-class NMR magnets, Supercond. Sci. Technol. 35 (3) (2022).
[55] J.F. Ellena, B. Liang, M. Wiktor, A. Stein, D.S. Cafiso, R. Jahn, L.K. Tamm, Dynamic structure of lipid-bound synaptobrevin suggests a nucleation-propagation mechanism for trans-SNARE complex formation, Proc. Natl. Acad. Sci. U. S. A. 106 (48) (2009) 20306–20311.
[56] J. Hazzard, T.C. Sudhof, J. Rizo, NMR analysis of the structure of synaptobrevin and of its interaction with syntaxin, J. Biomol. NMR 14 (3) (1999) 203–207.
[57] N.A. Lakomek, H. Yavuz, R. Jahn, A. Perez-Lara, Structural dynamics and transient lipid binding of synaptobrevin-2 tune SNARE assembly and membrane fusion, Proc. Natl. Acad. Sci. U. S. A. 116 (18) (2019) 8699–8708.
[58] A.V. Pobbati, A. Stein, D. Fasshauer, N- to C-terminal SNARE complex assembly promotes rapid membrane fusion, Science 313 (5787) (2006) 673–676.
[59] N. Bloembergen, R.V. Pound, Radiation damping in magnetic resonance experiments, Phys. Rev. 95 (1) (1954) 8–12.
[60] R. Ishima, Effects of radiation damping for biomolecular NMR experiments in solution: A hemisphere concept for water suppression, Concept. Magn. Reson. A 44a (5) (2015) 252–262.
[61] D. Shishmarev, G. Otting, Radiation damping on cryoprobes, J. Magn. Reson. 213 (1) (2011) 76–81.
[62] J.P. Loria, M. Rance, A.G. Palmer, Transverse-relaxation-optimized (TROSY) gradient-enhanced triple-resonance NMR spectroscopy, J. Magn. Reson. 141 (1) (1999) 180–184.
[63] V. Sklenar, Suppression of radiation damping in multidimensional nmr experiments using magnetic-field gradients, J. Magn. Reson. A 114 (1) (1995) 132–135.
[64] M. Sattler, J. Schleucher, C. Griesinger, Heteronuclear multidimensional NMR experiments for the structure determination of proteins in solution employing pulsed field gradients, Prog Nucl Mag Res Sp 34 (2) (1999) 93–158.
[65] P. Schanda, H. Van Melckebeke, B. Brutscher, Speeding up three-dimensional protein NMR experiments to a few minutes, J. Am. Chem. Soc. 128 (28) (2006) 9042–9043.
[66] P. Schanda, B. Brutscher, Very fast two-dimensional NMR spectroscopy for real-time investigation of dynamic events in proteins on the time scale of seconds, J. Am. Chem. Soc. 127 (22) (2005) 8014–8015.
[67] D. Joseph, C. Griesinger, Optimal control pulses for the 1.2-GHz (28.2-T) NMR spectrometers, Sci. Adv. 9 (45) (2023) eadj1133.
[68] A.G. Palmer, J. Cavanagh, P.E. Wright, M. Rance, Sensitivity improvement in proton-detected 2-dimensional heteronuclear correlation NMR-spectroscopy, J. Magn. Reson. 93 (1) (1991) 151–170.
[69] K. Pervushin, R. Riek, G. Wider, K. Wuthrich, Attenuated T-2 relaxation by mutual cancellation of dipole-dipole coupling and chemical shift anisotropy indicates an avenue to NMR structures of very large biological macromolecules in solution, Proc. Natl. Acad. Sci. U. S. A. 94(23) (1997) 12366-12371.
[70] M. Salzmann, G. Wider, K. Pervushin, K. Wuthrich, Improved sensitivity and coherence selection for [N-15, H-1]-TROSY elements in triple resonance experiments, J. Biomol. NMR 15 (2) (1999) 181–184.
[71] G. Wider, Technical aspects of NMR spectroscopy with biological macromolecules and studies of hydration in solution, Prog. Nucl. Magn. Res. Spectr. 32 (1998) 193–275.
[72] H. Geen, R. Freeman, Band-selective radiofrequency pulses, J. Magn. Reson. 93 (1) (1991) 93–141.
[73] F.A.A. Mulder, R.A. de Graaf, R. Kaptein, R. Boelens, An off-resonance rotating frame relaxation experiment for the investigation of macromolecular dynamics using adiabatic rotations, J. Magn. Reson. 131 (2) (1998) 351–357.
[74] M. Garwood, Y. Ke, Symmetrical pulses to induce arbitrary flip angles with compensation for Rf inhomogeneity and resonance offsets, J. Magn. Reson. 94 (3) (1991) 511–525.
[75] X. Shao, T.C. Sudhof, J. Rizo, Assignment of the 1H, 15N and 13C resonances of the calcium-free and calcium-bound forms of the first C2-domain of synaptotagmin I, J. Biomol. NMR 10 (3) (1997) 307–308.
[76] F. Delaglio, S. Grzesiek, G.W. Vuister, G. Zhu, J. Pfeifer, A. Bax, Nmrpipe - a multidimensional spectral processing system based on UNIX pipes, J. Biomol. NMR 6 (3) (1995) 277–293.
[77] H. Desvaux, P. Berthault, Study of dynamic processes in liquids using off-resonance RF irradiation, Prog. Nucl. Magn. Res. Spectr. 35 (4) (1999) 295–340.
[78] A.G. Palmer, F. Massi, Characterization of the dynamics of biomacromolecules using rotating-frame spin relaxation NMR spectroscopy, Chem. Rev. 106 (5) (2006) 1700–1719.
[79] D.M. Lemaster, Isotope labeling in solution protein assignment and structural-analysis, Prog. Nucl. Magn. Res. Spectr. 26 (1994) 371–419.

[80] S. Grzesiek, P. Wingfield, S. Stahl, J.D. Kaufman, A. Bax, 4-Dimensional N-15-separated noesy of slowly tumbling perdeuterated N-15-enriched proteins - application to Hiv-1 Nef, J. Am. Chem. Soc. 117 (37) (1995) 9594–9595.
[81] A. Eletsky, A. Kienhofer, K. Pervushin, TROSY NMR with partially deuterated proteins, J. Biomol. NMR 20 (2) (2001) 177–180.
[82] M. Gairi, A. Dyachenko, M.T. Gonzalez, M. Feliz, M. Pons, E. Giralt, An optimized method for (15)N R(1) relaxation rate measurements in non-deuterated proteins, J. Biomol. NMR 62 (2) (2015) 209–220.
[83] P.J. Nichols, I. Falconer, A. Griffin, C. Mant, R. Hodges, C.J. McKnight, B. Vogeli, L. Vugmeyster, Deuteration of nonexchangeable protons on proteins affects their thermal stability, side-chain dynamics, and hydrophobicity, Protein Sci. 29 (7) (2020) 1641–1654.
[84] J.S. Mugridge, R.G. Bergman, K.N. Raymond, Does size really matter? The steric isotope effect in a supramolecular host-guest exchange reaction, Angew. Chem., Int. Ed. 49 (21) (2010) 3635–3637.
[85] P. Cioni, G.B. Strambini, Effect of heavy water on protein flexibility, Biophys. J. 82 (6) (2002) 3246–3253.
[86] W. Adamski, N. Salvi, D. Maurin, J. Magnat, S. Milles, M.R. Jensen, A. Abyzov, C. J. Moreau, M. Blackledge, A unified description of intrinsically disordered protein dynamics under physiological conditions using NMR spectroscopy, J. Am. Chem. Soc. 141 (44) (2019) 17817–17829.
[87] N. Salvi, A. Abyzov, M. Blackledge, Multi-timescale dynamics in intrinsically disordered proteins from NMR relaxation and molecular simulation, J. Phys. Chem. Lett. 7 (13) (2016) 2483–2489.
[88] N. Salvi, A. Abyzov, M. Blackledge, Solvent-dependent segmental dynamics in intrinsically disordered proteins, Sci. Adv. 5 (6) (2019).
[89] A. Abyzov, E. Mandelkow, M. Zweckstetter, N. Rezaei-Ghaleh, Fast motions dominate dynamics of intrinsically disordered tau protein at high temperatures, Chem. Eur. J. 29 (17) (2023).
[90] N. Rezaei-Ghaleh, G. Parigi, M. Zweckstetter, Reorientational dynamics of amyloid-beta from NMR spin relaxation and molecular simulation, J. Phys. Chem. Lett. 10 (12) (2019) 3369–3375.
[91] D. Kurzbach, G. Kontaxis, N. Coudevylle, R. Konrat, NMR spectroscopic studies of the conformational ensembles of intrinsically disordered proteins, Adv. Exp. Med. Biol. 870 (2015) 149–185.
[92] S. Kim, K.P. Wu, J. Baum, Fast hydrogen exchange affects N-15 relaxation measurements in intrinsically disordered proteins, J. Biomol. NMR 55 (3) (2013) 249–256.
[93] M.L. Gill, R.A. Byrd, A.G. Palmer, Dynamics of GCN4 facilitate DNA interaction: a model-free analysis of an intrinsically disordered region, Phys. Chem. Chem. Phys. 18 (8) (2016) 5839–5849.
[94] J.P. Brady, P.J. Farber, A. Sekhar, Y.H. Lin, R. Huang, A. Bah, T.J. Nott, H. S. Chan, A.J. Baldwin, J.D. Forman-Kay, L.E. Kay, Structural and hydrodynamic properties of an intrinsically disordered region of a germ cell-specific protein on phase separation, Proc. Natl. Acad. Sci. U. S. A. 114 (39) (2017) E8194–E8203.
[95] D.S. Libich, V. Tugarinov, G.M. Clore, Intrinsic unfoldase/foldase activity of the chaperonin GroEL directly demonstrated using multinuclear relaxation-based NMR, Proc. Natl. Acad. Sci. U. S. A. 112 (29) (2015) 8817–8823.
[96] Z. Solyom, P.X. Ma, M. Schwarten, M. Bosco, A. Polidori, G. Durand, D. Willbold, B. Brutscher, The disordered region of the HCV protein NS5A: Conformational dynamics, SH3 binding, and phosphorylation, Biophys. J. 109 (7) (2015) 1483–1496.
[97] S.C. Chiliveri, Y. Shen, J.L. Baber, J.F. Ying, V. Sagar, G. Wistow, P. Anfinrud, A. Bax, Experimental NOE, chemical shift, and proline isomerization data provide detailed insights into amelotin oligomerization, J. Am. Chem. Soc. 145 (32) (2023) 18063–18074.
[98] T. Gruber, M. Lewitzky, L. Machner, U. Weininger, S.M. Feller, J. Balbach, Macromolecular crowding induces a binding competent transient structure in intrinsically disordered Gab1, J. Mol. Biol. 434 (5) (2022).
[99] K. Kämpf, S.A. Izmailov, S.O. Rabdano, A.T. Groves, I.S. Podkorytov, N. R. Skrynnikov, What drives N spin relaxation in disordered proteins? Combined NMR/MD study of the H4 histone tail, Biophys. J. 115 (12) (2018) 2348–2367.
[100] N. Salvi, V. Zapletal, Z. Jasenakova, M. Zachrdla, P. Padrta, S. Narasimhan, T. Marquardsen, J.M. Tyburn, L. Zidek, M. Blackledge, F. Ferrage, P. Kaderavek, Convergent views on disordered protein dynamics from NMR and computational approaches, Biophys. J. 121 (20) (2022) 3785–3794.
[101] S. Milles, D. Mercadante, I.V. Aramburu, M.R. Jensen, N. Banterle, C. Koehler, S. Tyagi, J. Clarke, S.L. Shammas, M. Blackledge, F. Grater, E.A. Lemke, Plasticity of an ultrafast interaction between nucleoporins and nuclear transport receptors, Cell 163 (3) (2015) 734–745.
[102] S. Naudi-Fabra, M. Tengo, M.R. Jensen, M. Blackledge, S. Milles, Quantitative description of intrinsically disordered proteins using single-molecule FRET, NMR, and SAXS, J. Am. Chem. Soc. 143 (48) (2021) 20109–20121.
[103] A. Borgia, M.B. Borgia, K. Bugge, V.M. Kissling, P.O. Heidarsson, C.B. Fernandes, A. Sottini, A. Soranno, K.J. Buholzer, D. Nettels, B.B. Kragelund, R.B. Best, B. Schuler, Extreme disorder in an ultrahigh-affinity protein complex, Nature 555 (7694) (2018) 61–66.
[104] C. Fernandez, G. Wider, TROSY in NMR studies of the structure and function of large biological macromolecules, Curr. Opin. Struct. Biol. 13 (5) (2003) 570–580.
[105] A.G. Tzakos, C.R. Grace, P.J. Lukavsky, R. Riek, NMR techniques for very large proteins and RNAs in solution, Annu. Rev. Biophys. Biomol. Struct. 35 (2006) 319–342.